This is the peer-reviewed, final accepted version for American Mineralogist, published by the Mineralogical Society of America.
The published version is subject to change. Cite as Authors (Year) Title. American Mineralogist, in press.
DOI: https://doi.org/10.2138/am-2022-8223. http://www.minsocam.org/

Revision 4 Characteristics and formation of corundum within syenite in the Yushishan rare metal deposits in the northeastern Tibetan Plateau

JIANHUA LIU[1], SHUYUN CAO[1*], DINGKUI ZHOU[1], XIAOWEN LI[1], YU WU[2], HAOBO WANG[1] AND WENXUAN LI[1]

[1]State Key Laboratory of Geological Processes and Mineral Resources, School of Earth Sciences, China University of Geosciences, Wuhan 430074, China
[2]Beijing Geological Research Institute of Nuclear Industry,100029

ABSTRACT

Corundum is relatively rare found in situ within the alkali syenite. The corundum-bearing syenite was firstly found in the Yushishan rare metal deposits of the eastern section of the Altyn Tagh fault in the northeastern Tibetan Plateau, but the characteristics and formation of corundum remain unknown. We describe a corundum-bearing syenite dike emplaced in biotite plagioclase gneiss that suffered overprinted deformation with characteristics of mylonitization. The corundum crystals have variable grain sizes, and the largest ones are up to megacrysts with growth zoning. The corundum crystals contain a variety of mineral inclusions that are divided into primary and secondary mineral inclusions. The primary mineral inclusions within the corundum include variable contents of Fe-Ti oxides needles, ilmenite, zircon, monazite-(Ce), potassium feldspar, pyrochlore, columbite-(Fe), magnetite, samarskite-(Y), and pyrite that indicate corundum crystallized in peraluminous Zr-rich and Si-poor alkali rock with variable TiO_2-contents. Secondary mineral inclusions include Zn-rich hercynite, ilmenite, magnetite, annite, fluorapatite, and intergrowth of ilmenite with columbite-(Fe) and goethite which reveal late-stage influx of Zn-, Ti-, Fe-, and F-bearing fluids into corundum that caused metasomatism and element migration/precipitation. The trace element analysis of corundum shows high Fe and Ga contents and low Mg and Cr contents that are consistent with the characteristics of corundum of magmatic origin. The trace element characteristics and the oxygen isotopes (6.2‰–8.2‰) results indicate that corundum crystallized in melts with the involvement of Al-rich and Si-poor crustal material.

Key words: syenite, corundum, mineral inclusions, trace element, oxygen isotopes

INTRODUCTION

Corundum (Al_2O_3) is a relatively rare mineral that becomes colored ruby or sapphire when trace elements (Cr, Fe, Ti, Mg, V and Si, etc.) are substituted in the aluminum oxide crystal lattice (e.g., Hughes 1997; Emmett et al. 2003, 2017; Peretti et al. 2008; Schwarz et al. 2008; Rossman 2009). The crystallization of corundum requires unusual geochemical conditions of low silica activity combined with high aluminum content in some metamorphic and magmatic rocks (Giuliani et al. 2014a). Up to now, the corundum sources have received various levels of description in geological and gemological literatures (e.g., Hughes 1997; Simonet et al. 2008; Giuliani et al. 2014a; Sorokina et al. 2021). Corundum is encountered in a range of rocks via several different petrogenetic processes (Simonet et al. 2008; Giuliani et al. 2014a, and references therein) and the global distribution of corundum (sapphire) deposits is closely linked to continent-continent collision, rift, and less commonly subduction environments (Graham et al. 2008; Simonet et al. 2008; Stern et al. 2013; Meng et al. 2018; Zhang et al. 2018; Sorokina et al. 2021). Therefore, the presence of corundum is not only economically valuable, but also is an important indicator of specific geological events and processes.

According to the geological occurrence, Simonet et al. (2008) classified corundum deposits into primary and "secondary" deposits. In primary deposits corundum crystallizes during metamorphic or igneous process, corundum is still in the same rock that it crystallized from. In "secondary" deposits, corundum is a clast of detrital origin or a xenocryst in lava, corundum occurs as an inherited mineral that formed in a different petrogenetic setting compared to where it is deposited now (Rakotondrazafy et al. 2008; Palke et al. 2017). In sedimentary deposits, corundum is frequently extracted from gem-bearing alluvium and eluvium. Corundum crystals are present as clasts inherited from other rock types of deposits as in eastern Australia (Coenraads 1992; Zaw et al. 2006), South-East Asia (Guo et al. 1996, Graham et al. 2008; Khamloet et al. 2014), Europe (Upton et al. 1999; Uher et al. 2012; Baldwin et al. 2017), and USA (Palke et al. 2017).

Corundum is found commonly in metamorphic rocks of varied lithologies in a wide range of pressure and temperature conditions (Garnier et al. 2008; Hattori et al. 2010; Dzikowski et al. 2014; Yakymchuk and Szilas 2017). Metamorphic corundum crystallizes as a result of isochemical metamorphic reactions in alumina-rich (e.g., aluminous gneisses and granulites) or silica-poor (e.g., marbles) rocks commonly associated with aluminous minerals such as garnet, spinel, sapphirine, cordierite, and mainly stable at P and T conditions ranging from amphibolite to granulite facies (Riesco et al. 2005; Garnier et al. 2008; Simonet et al. 2008; Dzikowski et al. 2014; Yakymchuk and Szilas 2017; Huang et al. 2021). The crystallization of metasomatic corundum is directly related to the introduction of reactive fluids or the accidental contact between two chemically different rocks, when silica-poor rocks (e.g., marble, amphibolite and ultramafic rocks) and aluminosilicate rocks (e.g., granitic pegmatites, Al-rich gneisses) come into direct contact, metasomatic desilication and crystallization of corundum occur on a small scale (Simonet et al. 2008; Meng et al. 2018; Yakymchuk and Szilas 2017; Zhang et al. 2018). Moreover, anatexis of quartz-poor aluminous protoliths were also reported (Mazzone and Stephen 1989; Cartwright and Barnicoat 2010; Palke et al. 2017; Li et al. 2020).

Magmatic corundum crystallizes directly from the melt as an accessory mineral at the deep crustal or upper mantle levels and is commonly captured by other deep-sourced magmas (e.g., alkaline basalt, lamprophyre) (Guo et al. 1996; Song and Hu 2009; Sutherland et al. 2009; Palke et al. 2016; Baldwin et al. 2017). Thus, magmatic corundum is mostly exposed at the surface as xenoliths and xenocrysts (Guo et al. 1996; Garnier et al. 2005; Palke et al. 2016; Baldwin et al. 2017). In plutonic rocks, syenite and nepheline syenite are typical rock types that corundum can directly crystallize from the magmatic melt. There are a few examples of in-situ corundum-bearing igneous rocks including the albitite dikes of Espéchère and Urdach in the western Pyrenees (France), which intruded into serpentinized lherzolite, are of mantle origin (Monchoux et al. 2006; Pin et al. 2006); Nepheline syenite pegmatites within an alkaline belt in Ontario, Canada (Moyd 1949; Kievlenko 2003); In Garba Tula, central Kenya, a leucocratic corundum- bearing monzonite dike in contact with biotite-hornblende gneiss, the monzonite is of mantle origin revealed by Sr–Nd isotopic data (Simonet et al. 2004); Syenite dike intruded into weathered gneiss in the Baw Mar mine, Mogok, Myanmar (Kan-Nyunt et al. 2013; Soonthorntantikul et al. 2017), and syenite pegmatites in the Ilmenogorsky alkaline complex of the southern Urals, Russia (Sorokina et al. 2017, 2021). Moreover, other examples were also found in sapphire-bearing syenite/anorthoclasite as xenoliths in the alkali basalts from Scotland (Upton et al. 1999), France (Giuliani et al. 2009), Slovakia (Uher et al. 2012) and Madagascar (Rakotosamizanany et al. 2014) indicating a syenitic origin. However, in situ occurrences where the corundum is still inside their host syenite are rarely found, which limit the comprehensive and in-depth study of the characteristics and genesis of magmatic corundum, the origin of corundum in syenite remains unclear.

In this contribution, we firstly present detailed results of meso- and micro-structures, petrology, mineral inclusions, trace elements and oxygen isotopes of corundum in syenite from the Yushishan metamorphic massif, a newly explored rare metal deposit in eastern North Altyn Tagh. The corundum grains contain abundant mineral inclusions that were divided into primary and secondary groups, which record two stages of geological processes. The trace element and oxygen isotope analyses are consistent with the characteristics of corundum of syenitic origin. Furthermore, the Al-rich and Si-poor crustal material were involved during the formation of corundum. These findings may provide new insights into in-situ corundum found in igneous rocks of syenitic composition.

GEOLOGICAL SETTING

The Yushishan metamorphic massif is a newly explored rare metal (e.g., Nb and Ta) deposit located at the intersection of the Altyn and Qilian tectonic belts at the northeastern margin of the Tibetan Plateau (Fig. 1a). The Yushishan massif is bounded by the Altyn strike-slip fault; the northern part of the Yushishan massif belongs to the Dunhuang Block, and the southern part represents the northern edge of the Qaidam Basin (Zhang et al. 2015) (Fig. 1b). The Dunhuang block is suggested to belong to the stable Precambrian metamorphic basement of the Dunhuang-Alxa craton (Lu et al. 2008; He et al. 2013; Zhang et al. 2013; Zong et al. 2013). Recent studies on high-grade metamorphic rocks such as high-pressure mafic granulites, amphibolites and eclogites exposed in the Dunhuang area indicate that the Dunhuang Block is a part of the Central Asian Orogenic Belt (Zong et al. 2012; Zhao et al. 2016; Pham et al. 2018; Zhao and Sun 2018). The eastern margin is the Central-South Qilian block, and the Hongliugou-Lapeiquan ophiolite mélange belt lies to the west. The study area is located in the Aksay area in the eastern section of the Hongliugou-Lapeiquan ophiolite belt, which starts from Hongliugou at the northern edge of the Altun orogenic belt in the west, and extends eastward to Lapeiquan, and spreads along the main Altyn Tagh fault through Annanba, Aksay and Su Bei County (Fig. 1b). Recent studies have shown that the Hongliugou-Lapeiquan ophiolite was formed in the Early Paleozoic, suggesting that an ancient ocean existed in the North Altun region during the Early Paleozoic (Liu 1999; Lu et al. 2008; Yang et al. 2008; Wu et al. 2009; Wang et al. 2018). The tectono-magmatic evolution of the Yushishan massif remains unclear.

The Yushishan massif experienced pre-Caledonian and Caledonian North Altun subduction-collisional orogeny and overprinted a left-lateral strike-slip movement of the Altyn Tagh fault since the Himalayan period (Liu et al. 2007). The exposed rock strata in the Yushishan massif include the Cambrian-Ordovician Lapeiquan Group, the Paleoproterozoic Dakendaban Group, the Jixian-Qingbaikou Period Binggounan Formation, and the Changchengian Period Aoyougou Formation, among which the Changchengian Period Aoyougou Formation is the primary exposed stratum in the study area (Fig. 2a). The principal metamorphic rocks exposed in the Yushishan are mylonitic gneisses (principally composed of banded, augen, and foliated migmatitic gneisses), amphibolite, marble, serpentinite, schists, and minor quartzite. The high-temperature metamorphic assemblages (up to amphibolite or granulite facies) preserved in the study area include almandine, staurolite, and sillimanite in schists; tremolite, diopside, olivine, calcite, and dolomite in marbles; and amphibole, garnet, and plagioclase in amphibolites. The magmatic rock types in the region are primarily Ordovician acidic rocks, followed by medium-basic rocks, which primarily appear in the northwest and southwest sides of the Yushishan massif and include quartz diorite, granodiorite, biotite monzogranite, syenite, and gabbro (Yu et al. 2015; Jia et al. 2016).

The metamorphic rocks show intense ductile deformation with well-developed foliation that bears a strong sub-horizontal stretching lineation parallel to the NNW-SSE trend. The shear criteria indicates that the metamorphic rocks underwent intense left-lateral ductile shearing. The occurrence of serpentinized marble, epidote scratches, and multi-period quartz veins in the study area indicates strong fluid activity (Li et al. 2021).

METHODS

Cathodoluminescence

The CL images were obtained on polished thin sections of corundum-bearing syenite at the School of Earth Sciences of the China University of Geosciences (Wuhan) using a cathodoluminescence instrument CLF-2 produced by Beacon Innovation INTL Company. The CL instrument was mounted on a regular petrographic microscope with a working distance of 12-15 mm. The polished thin sections were put on the vacuum chamber which was attached to the microscope stage. The maximum vacuum is 0.0025 mbar and voltage of the electron gun is up to 30 kV.

Scanning electron microscope (SEM) analysis

Optical microstructural observations and measurements were primarily conducted on thin sections of corundum-bearing syenite and raw corundum megacrysts. All samples were cut parallel to the kinematic XZ section (i.e., X parallel to the mineral stretching lineation and, where visible, Y normal to the weak foliation). In-situ trace elements were tested on these thin sections. Raw corundum megacrysts were broken to pieces, and fresh flat surfaces were selected and carbon-coated for detailed morphological characteristics analysis. Field scanning electron microscopy studies were performed at the School of Earth Sciences of the China University of Geosciences (Wuhan) using a new Sigma 300VP FEG-SEM field emission scanning electron microscope with an energy dispersive spectrometer (EDS) detector for detailed sub-microscopic microstructure analysis. Field scanning electron microscopy was performed to obtain the backscatter diffraction images with spot size of 6.0 mm. The beam current and accelerating voltage were set at 15 nA and 20 kV, respectively; The work distance was ~12 mm.

Corundum trace element compositions analysis

Trace element compositions of corundum were measured using laser ablation inductively coupled plasma-mass spectrometry (LA-ICP-MS) at Wuhan Sample Solution Analytical Technology Co., Ltd., Wuhan, China. Laser sampling was performed using a GeolasPro laser ablation system that consisted of a COMPexPro 102 ArF excimer laser (wavelength of 193 nm and maximum energy of 200 mJ) and a MicroLas optical system. An Agilent 7700e ICP-MS instrument was used to acquire the mass signal intensities. Helium was used as a carrier gas. Argon was used as the make-up gas and mixed with the carrier gas via a T-connector before entering the ICP. A "wire" signal smoothing device was included in the laser ablation system. The spot size and frequency of the laser were set to 32μm and 5 Hz, respectively. The trace element compositions of the minerals were calibrated against various reference materials (BHVO-2G, BCR-2G, BIR-1G, and NIST SRM610) without using an internal standard (Liu et al. 2008). Trace elements of interest measured are ^{24}Mg, ^{47}Ti, ^{51}V, ^{52}Cr, ^{55}Mn, ^{57}Fe and ^{71}Ga. The relative standard deviation (RSD) for the trace element determined was 5-10%. An Excelbased software ICPMSDataCal was used to perform offline selection and integration of background and analyzed signals, time-drift correction, and quantitative calibration for trace element analysis (Liu et al. 2008). The measured concentrations of QCM (quality control material) agree for all elements within 15% of preferred values (Jochum et al. 2011). Table 1 presents the results.

Isotope Ratio Mass Spectrometer (IRMS) for oxygen isotope composition analysis

Six samples of corundum from syenite were collected, corundum samples were crushed to fine powder below 200 mesh firstly, then clean corundum grains were hand-picked under a binocular microscope to avoid the contamination of mineral inclusions. Oxygen was extracted through complete reaction of ~1 mg of powdered corundum, heated by an IR-laser in the presence of BrF_5. The released oxygen was then purified at two cryogenic traps with liquid nitrogen and on absorber with KBr. A MAT-253 gas isotope ratio mass spectrometer was used to measure the oxygen isotope composition of corundum at the Beijing Geological Research Institute of Nuclear Industry. The precision and accuracy of quartz standards (GBW-04409 and GBW-0441 quartz) were ±0.2‰ (1σ). Replicate oxygen isotope analyses of the standard used had an average precision of ±0.1‰ for $\delta^{18}O$. The accuracy of $\delta^{18}O$ values was better than 0.2‰; $\delta^{18}O$ values for GBW-04409 and GBW-0441 were 11.11±0.06‰ and 1.75±0.08‰, respectively. The data were reported in conventional delta notation ($\delta^{18}O$, expressed in per mil, ‰) relative to the Vienna Standard Mean Ocean Water (Table 2).

RESULTS

Petrology of corundum-bearing syenite

In the Yushishan metamorphic massif, deformation and accompanying anatectic melting can be described as sinistral ductile shearing under granulite-facies high temperature metamorphic conditions. Ductile deformation is characterized by sub-horizontal stretching lineation, sub-vertical foliation, and folds/thrust with lineation-parallel hinges in the mylonites. Corundum-bearing syenites are ubiquitous and occur as dikes emplaced in biotite plagioclase gneiss in the southwest of the Yushishan metamorphic massif. The dike extends up to 1000 m with a width of 15–25 m and dips NWW at angles of 45–55° (Fig. 2b and Fig. 3a). The contact interface between corundum-bearing syenite and the layered biotite plagioclase gneiss host rock is clear and straight (Fig. 3c). Meta-gabbro occurs as lens-shape xenoliths in both biotite plagioclase gneiss and corundum-bearing syenite (Fig. 2b and Fig. 3b). The corundum content in syenite is 5%–30%, and the grain size ranges widely from 0.5 to 4 cm, some corundum grains reach megacryst size. Most of the corundum crystals are euhedral, commonly displaying a hexagonal prismatic habit or barrel-like shaped. The corundum is primarily light blue or grey, with a glassy luster (Fig. 3d). Moreover, the corundum-bearing syenite suffered strong shear deformation and show characteristics of mylonitization and the corundum porphyroclasts are significantly rotated (Figs. 3e–f). Regular fine-scale hexagonal growth zoning was observed in the cross-section perpendicular to the corundum column, which alternatively appeared as brown and light blue oscillatory zonation likely due to Ti-Fe oxide micro-inclusions (Fig. 3g).

The corundum-bearing syenite is composed of albite, orthoclase, annite, muscovite, corundum, and garnet with accessory minerals (e.g., magnetite, monazite-(Ce), pyrite, and zircon) (Figs. 4a–g). Oriented, coarse-grained corundum are embedded in a fine-grained matrix. The corundum grains present distinct shape types according to their [0001]-axis orientations and display hexagonal or prismatic shapes (Fig. 4a). In these corundum grains, obvious polysynthetic twinning are readily visible in most samples; The replacement of alkali feldspars by muscovite was observed along the contact with corundum: corundum+K-feldspar+H_2O↔ muscovite (Icenhower and London 1995; Raith et al. 2010) (Figs. 4a–b). There are also domains in which corundum shows coronitic replacement partially by dark green Zn-rich hercynite (Figs. 4c–d). Garnet (almandine-spessartine) grains in the corundum-bearing syenite display highly irregular grain boundaries and exhibit a metastable state with surrounding plagioclase and annite. The reacting relationship between corundum and garnet was not observed (Fig. 4e). Some corundum grains also display microfractures healed by late-stage muscovite (Fig. 4f). In the cathodoluminescence (CL) image, the fine-grained K-feldspar has a blue luminescence, albite is green, and the black or dark areas are mostly corundum, annite, muscovite, garnet, and spinel coronas (Figs. 4f–g).

Mineral inclusions within corundum

We used polished thin sections and raw corundum megacrysts to better observe and study the surface features and internal characteristics of the mineral inclusions within the corundum, which were categorized into primary and secondary groups according to their genetic links with the host corundum. Microscopic observations were used to separate and classify the primary and secondary mineral inclusions, especially when the morphological characteristics of the inclusions were also clearly observed under scanning electron microscope. Inclusions are interpreted to be primary if they are completely enclosed within the corundum with regular grain shape and are not located at any visible cracks, twin boundaries, or cleavages. On the other hand, those inclusions have restricted grain shapes by cracks, twin boundaries or cleavages in the corundum and have xenomorphic grain shapes are interpreted to be secondary.

Optical microscope observations of mineral inclusions

Optical microscope observations revealed that the primary mineral inclusions within corundum grains include Fe-Ti oxides, fine-grained zircon, pyrochlore, magnetite, pyrite, Zn-rich hercynite, K-feldspar, and samarskite-(Y) (Fig. 5). Among these mineral inclusions, magnetite, zircon, and feldspar are the most common ones. The Fe-Ti oxides presents oriented needle-like shapes with a brownish color and lies in the basal plane of corundum and the needle axes parallel to three (10-10) directions. The needles commonly appear in angular bands (intersecting themselves at an angle of 60°/120°) and correspond to the growth zones of the corundum crystals (Fig. 3g). The lengths reach 100 μm, and the widths are approximately 1 μm. The distribution of the needle-like inclusions often varies in different corundum grains and within the same corundum which display core and margin inhomogeneous characteristics (Figs. 5a–c).

The composition of the oriented needle-like inclusions in the corundum was mapped by scanning electron microscopy (SEM) with energy dispersive spectrometry (EDS) scanning. Because the depth of exposure of such needle-like inclusions varies in the corundum, only a few needle-like inclusions present clear correlation with Ti and Fe distribution (Figs. 5d–f). The results indicate that needle-like inclusions are Fe-Ti oxides. Thus, the oriented needle-like inclusions are solid solutions of hematite (Fe_2O_3) and ilmenite ($FeTiO_3$), most likely ilmenite. The spinel (Zn-rich hercynite) inclusions show a dark-greenish color with an irregular shape, suggesting post-genetic genesis (Fig. 5g). Zircon inclusions are characterized by fine-grained (5–15μm) and bipyramidal crystals with inhomogeneous but locally more intensive distribution (Fig. 5h). Black opaque magnetite crystals are euhedral to subhedral. Pyrochlore, which is dark reddish-brown in color and spindle-shaped, is also found in corundum grains (Fig. 5i). Small feldspar (orthoclase) grains (ca. 20 μm in length) have euhedral to subhedral crystal shapes that are K-rich with low Na and Ca content (Fig. 5j). Sulfide inclusions are primarily pyrites that display a light-yellow color and characteristic zoning under reflected light with outer zone replaced by goethite (Fig. 5k). Columnar samarskite-(Y) crystals were also observed with radial cracks around them (Fig.5l).

Scanning electron microscopy (SEM) observations of mineral inclusions

Scanning electron microscope was used to observe and classify the morphological characteristics of the mineral inclusions. The primary mineral inclusions include zircon, monazite-(Ce), columbite-(Fe), ilmenite, magnetite, and samarskite-(Y). Zircon inclusions were fine-grained and euhedral (Fig. 6a). Monazite-(Ce) has a columnar shape, and fine-grained zircons are often inserted into larger monazite-(Ce) (Fig. 6b). Magnetite inclusions with rounded grain boundaries have relatively large grain sizes (200–500 μm) and developed microfractures (Fig. 6c), whereas fine-grained magnetite aggregates occur less frequently (Fig. 6d). Primary ilmenite inclusions display rhombic crystals and are fine-grained and concentrated to form aggregates (not needle-like) (Fig. 6e). Samarskite-(Y) is also found with nearly columnar shape (Fig. 6f).

Secondary mineral inclusions include spinel, goethite, magnetite, annite, fluorapatite, pyrite, and intergrowth of ilmenite with columbite-(Fe). These mineral inclusions are commonly constrained by the cleavage and twin boundaries of the corundum. Significant reaction characteristics are also typical clues for identifying secondary mineral inclusions. Secondary inclusions of ilmenite occur as three groups of thin veins that have similar orientation of corundum twins, indicating formation after corundum crystallization (Fig. 7a). Secondary magnetite inclusions developed as aggregated strips (Fig. 7b). The spinel is primarily Zn-rich hercynite, which is characterized by discontinuous grid-like veins, indicating that the Zn-rich hercynites are late-stage mineral inclusions (Fig. 7c). Annite grains with cleavage flakes appear inside the corundum and at the edge of the corundum extending outside the corundum (Fig. 7d). The apatite mineral inclusions in this study contain F-elements belonging to fluorapatite present irregular boundaries (Fig. 7e). The pyrite has a nearly wedge- or tailed-shape; goethite is layered between pyrite and corundum. The goethite layers are parallel with the tail of the pyrite, which indicate that the goethite formed as a product of the late alternation of pyrite (Figs. 7f–g). Columbite-(Fe) intergrowth with ilmenite in patchy and the whole grains is columnar-shaped. In the SEM images, the grayish and white phases were ilmenite and columbite-(Fe), respectively (Figs. 7h–i).

Trace element geochemistry

Trace element contents of corundum within syenite were measured by in situ LA-ICP-MS on six samples from the Yushishan massif. Table 1 presents the results. The data show that the amount of Fe ranges from 8411–11627 μg/g (average 9607 μg/g). The samples have high Ga content of 161–212 μg/g (average 182 μg/g) but low Mg content from ~b.d.l to 18.0 μg/g; the high Ga/Mg ratios range from 10–168. The Ti concentration ranges from 9 to 771 μg/g; Fe/Ti ratios range from 15–984. The Cr and Mn concentration are low (~b.d.l to 7.3 μg/g and ~b.d.l to 18.53 μg/g, respectively). The very low V contents ranges from ~b.d.l to 1.13 μg/g.

Oxygen isotope composition

$\delta^{18}O$ analysis of corundum is an important method for understanding the source origin of corundum-bearing rocks (Yui et al. 2003, 2006; Giuliani et al. 2005, 2007; Vysotskiy et al. 2015). Six selected corundum samples from the Yushishan massif were used to measure the oxygen isotope composition. The $\delta^{18}O$ values of corundum from the Yushishan massif ranged from 6.2‰–8.2‰. Table 2 lists the data from this study and previously obtained $\delta^{18}O$ values of magmatic corundum, the $\delta^{18}O$ values from some corundum deposits with serial data mainly choose the largest and the smallest values to get the complete range, and some special values were also included.

DISCUSSION

Origin of corundum in the Yushishan syenite

Corundum from different types of deposits have various trace element characteristics. The contents of Fe, Ti, Cr, Ga, Mg trace elements and element ratios (e.g., Ga/Mg and Ga*/Al= 10000 Ga/Al) in corundum (sapphire) are often used in gem-corundum classification (Peucat et al. 2007; Sutherland et al. 2008; Zwaan et al. 2015; Filina et al. 2019). Conundrum of magmatic origin typically contains higher Fe and Ga contents and lower Cr and Mg contents than corundum of metamorphic origin. The magmatic corundum has contents of Fe about 1800-13000 μg/g and Ga about 70-570 μg/g and low contents of Cr and Mg (usually < 40 μg/g), and the metamorphic corundum has contents of Fe <3000 μg/g and Ga <75 μg/g and enriched in Cr and Mg (usually > 60 μg/g) (Peucat et al. 2007). But in recent years, there is controversy about this separation, especially the low Ga contents also appeared in magmatic and/or anatectic sapphires (Sutherland et al. 2015; Palke et al. 2016) and the Cr content in corundum is alco connected to the crystal habits of corundum at various P-T conditions (Sorokina et al. 2016). The trace element classification schemes used to separate metamorphic, metasomatic, and magmatic sapphires ought to be careful.

The corundum from the Yushishan area has high Fe (8411–11627 μg/g) and Ga (161–212 μg/g) contents and low Mg content (~b.d.l to 18.0 μg/g). The low Mg content of corundum is usually related to its crystallization environment. Magmatic-origin related rocks (e.g., syenite) generally have lower Mg content than metamorphic-origin corundum, which is often associated with Mg-Fe-rich or ultramafic rocks. The Ti content ranges from 9–771 μg/g, the heterogeneous behavior of Ti values may be related to contaminations of needle-like ilmenite inclusions within the corundum, which is difficult to completely avoid during test for the frequent emergence of these needle-like ilmenite inclusions. Thus, we excluded these spots with obvious contamination in discriminant diagrams on Fig 8–Fig10. The Cr and V contents are significantly lower (~b.d.l to 7.3 μg/g and ~b.d.l to 1.13 μg/g, respectively). On the Fe vs. Ga/Mg diagram, the corundum from the Yushishan syenite belongs to the magmatic domain (Fig. 8) and differs significantly from corundum with metamorphic or metasomatic genesis. The Ga/Mg ratio of corundum in the study area has a larger range of variation than that in the Garba Tula syenite (Peucat et al. 2007), primarily due to the variation in the Mg content of corundum in the study area (~b.d.l to 18.0 μg/g).

Corundums from the Yushishan show similar Mg (~bdl-18.0 μg/g) contents compared to that from the Ilmen syenite pegmatites (Mg ranges from 0.9-7.5 μg/g). However, the corundum in the Yushishan syenite has a significantly higher Fe (8411–11627 μg/g) than that of the Ilmen syenite pegmatites (Fe ranges from 2614 μg/g to 3257 μg/g). Sapphires from the Garba Tula syenite and the Changle alkaline basalt show similar Fe content to the Yushishan corundum. The high Ga (161–212 μg/g) content and the Ga*/Al ratios of 3.1–4.1 of the Yushishan corundum are also consistent with the magmatic origin of the corundum (Ga*/Al = 2.5–5.3) (Peucat et al. 2007). Moreover, Palke et al. (2016) further suggest that the “magmatic” sapphires of Peucat et al. (2007) represent sapphires associated with alkalic or felsic magmas, but not necessarily encompass magmatic sapphires in general. The Ga*/Al ratios (3.1–4.1) of the Yushishan corundum is significantly different from that of the Yogo Gulch corundum (Ga*/Al = 0.7–0.9), which crystalized through the peritectic melting of kyanite (Plake et al.

2016). What's more, Corundum–leucosome-bearing gneiss has been reported from Ayyarmalai, Southern Granulite Terrain, India (Raith et al. 2010) and in the North Dabie complex zone of Central China (Li et al. 2020). The leucosomes occurred around the sites of nucleation and growth of peritectic corundum. These peraluminous anatexites usually contain alumina-rich phases (e.g., sillimanite, kyanite, and/or andalusite) related to muscovite dehydration-melting, which is inconsistent with microstructures and mineral assemblages displayed in the Yushishan samples (Fig. 4).

The FeO-Cr_2O_3-MgO-V_2O_3 vs. $FeO + TiO_2 + Ga_2O_3$ diagram is used to clarify the metamorphic vs. magmatic origins of corundum based on the distinct contents of trace elements in different corundum types (Giuliani et al. 2014b). The corundum from the Yushishan plot within the syenite domain, which overlaps the domains of corundum xenocrysts in Scottish alkali basalts, the sapphire xenocrysts in the Changle alkaline basalt from Shandong Province and sapphire in Garba Tula syenite (Fig. 9). In the Fe-Mg-Ti diagram (Fig. 10), corundum from the Yushishan syenite plots in the magmatic domain, in addition, as same as the data from other sources of corundum with magmatic genesis, the distribution of data points are mainly concentrated in the end member of Fe and has the trend of Fe-Ti variation. On the other hand, corundum in Montana underwent a partial melt process that presents a significant variation trend of Fe-Mg across the domains of magmatism and metamorphism (Palke et al. 2016, 2017). which is different from that of corundum in Yushishan.

Minerals inclusions related to two stages of geological processes

Stage I-Corundum crystallization from the syenitic magma. In the Yushishan corundum, the primary inclusions include very fine-grained zircon, monazite-(Ce), K-feldspar, pyrochlore, magnetite, samarskite-(Y), ilmenite, columbite-(Fe) and pyrite (Figs. 6a–f). These primary inclusions have an equilibrium mutual grain contact with the host corundum and are lack of reaction characteristics or restricted outlines. The inclusions were incorporated into the host corundum during crystal formation, indicating corundum-bearing syenite in the Yushishan originated from a highly evolved melt enriched in incompatible elements. Similar mineral inclusions in corundum were also reported in syenites from other regions. The mineral inclusions in syenite pegmatites from the Ilmen Mountains of Russia's South Urals including columbite-(Fe), zircon, alkali feldspar, monazite-(Ce), sub-micron grains of uraninite, muscovite and diaspore, and exsolved micron-sized needles of ilmenite were identified within the blue sapphire (Sorokina et al. 2017). In corundum-bearing albitite of western Pyrénées, France. Albite, muscovite, biotite, chlorite, epidote, zircon, titanite, ferro- and manganocolumbite, thorite, pyrochlore (s.l.), aeschynite-(Ce), rutile, ilmenite and magnetite were found associated with corundum (Monchoux et al. 2006). Moreover, similar mineral inclusions were also found within corundum from the Nezametnoye corundum deposit, Primorsky of Russia. The syngenetic mineral inclusions include rutile, zircon, albite, zinc-bearing hercynite, columbite, and fluorite (Pakhomova et al. 2006). Although there are also other few examples of in-situ corundum-bearing igneous rocks, these studies didn't provide detailed and typical mineral inclusions in corundum to be compared (Kievlenko 2003; Simonet et al. 2004; Soonthorntantikul et al. 2017). Therefore, it can be suggested that the corundum formed in syenitic melt in situ, which is consistent with the evidence of trace elements that corundum from the Yushishan syenite has a magmatic origin. In the corundum, the distribution of ilmenite needles is closely related to corundum growth zoning (Fig. 3g). Similar characteristics were usually reported (e.g., McGee 2005; Baldwin et al. 2017; Soonthorntantikul et al. 2017; Sorokina et al. 2017). Previous studies suggest that needle-like oxides (rutile-TiO_2, hematite-Fe_2O_3, and ilmenite-$FeTiO_3$) in corundum form through exsolution by slow cooling and often develop in magmatic or metamorphic corundum (Moon and Phillips 1984; Izokh et al. 2010; Khamloet et al. 2014; Palke and Breeding 2017). However, there is still controversy about the exsolution origin of those needle-like oxides in corundum (Palke and Breeding 2017). The uneven distribution of needle-like ilmenite may suggest a varying titaniferous environment but detailed in situ LA-ICP-MS trace elements measurement is needed. Overall, based on the occurrence of primary mineral inclusion suite, the Yushishan corundum has crystallized from a highly evolved zirconium- and alkali-rich silica-poor syenitic melt with varying TiO_2-contents.

Stage II-Fluid-infiltration metasomatism. Secondary mineral inclusions include Zn-rich hercynite, magnetite, annite, fluorapatite, intergrowth of columbite-(Fe) with ilmenite, goethite, and ilmenite, which have a disequilibrium mutual grain contact with the host corundum in the Yushishan syenite (Figs. 7a–i). These mineral inclusions commonly have reaction characteristics, or a regular outline restricted by the cleavage or twin plans of the host corundum that reflect the metamorphic reactions or fluid processes after the crystallization of the host corundum. Spinel with various end-member compositions is not only a common reacting production of corundum developed in corundum-bearing rocks, but also as mineral inclusions occur within corundum with a metamorphic origin at granulite facies conditions (Downes and Bevan 2002; Raith et al. 2010; Keller and Ague 2018). In this study, the Zn-rich hercynite minerals occur not only within corundum as secondary mineral inclusions (Fig.7c), but also appeared as metasomatic product of corundum (Figs. 4c-d). Similar characteristics were also reported by Pakhomova et al. (2006) in Nezametnoye of Russia, zinc-bearing hercynite is accessory to metasomatite and granitoid greisen. Raith et al. (2010) reported that in southern Madagascar the influx of Mg-, Si- and K-bearing fluids into the anorthite-corundum rocks caused significant metasomatic changes, leading to the formation of phlogopite and Mg-Al minerals (spinel and sapphirine). It is also reported that in spinel–chlorite–muscovite rocks within meta-ultramafites of Ilmen Mountains, South Urals. The spinel coronas around corundum were explained as product of metasomatic alteration (Sorokina et al. 2019). Other secondary mineral inclusions also provide further evidence for the existence of metasomatic fluid. The vein-like ilmenite presents patterns in three directions (Fig. 7a) are similar to the distribution of needle-like oriented ilmenite in corundum. The distribution of vein-like ilmenite is potentially controlled by the distribution of needle-like oriented ilmenite in the presence of fluid. Magnetite inclusions within corundum also display characteristics like those of the stripes. Thus, fluid-infiltration metasomatism can explain these phenomena through the movement of fluids along twin boundaries and/or corundum cleavage and chemically react with corundum to cause a mass transfer. During the fluid migration process, the precipitation of Fe and Ti lead to formation of vein-like ilmenite and magnetite stripes. Goethite appears at the rim of the pyrite, indicating the transformation of pyrite to goethite (Fig. 5k and Figs. 7f-g), which involves oxidation and the participation of water-containing fluids. In addition, intergrowth of ilmenite with columbite-(Fe) in patches were observed (Fig.7i), considering the composition of these two minerals they can be the pseudomorph of Nb-rich rutile. Fluorine could be a major factor controlling the mobilization and enrichment of Nb in magmatic and metasomatic processes, and it may increase Nb solubility in fluids or melts (Agangi et al. 2010; Estrade et al. 2014; Huang et al. 2018; Zhu et al. 2020). In the corundum-bearing syenite, the appearance of fluorite and fluorapatite also supports the existence of F-rich fluids to promote Nb mobilization, leading to the intergrowth of columbite-(Fe) with ilmenite in patches.

The mineral inclusions provide strong evidence that the Yushishan corundum crystallized from a highly evolved syenitic magma. After crystallization, the corundum underwent late-stage fluid-infiltration metasomatism, the influx of Zn-, Ti-, Fe-, and F-bearing fluids, which caused significant metasomatic changes and element precipitation. The changes are displayed by the characteristics of secondary mineral inclusions in the host corundum.

The possible source of corundum-bearing syenite

Several mechanisms have been proposed for the formation and origin of magmatic corundum. It is proposed that low-volume initial melting of amphibole-bearing mantle generates felsic magma enriched in volatile elements, allowing the crystallization of corundum and zircon (Sutherland et al. 1998). This model explains the enrichment of Hf, Nb, and Ta, which are generally observed in minerals cogenetic with corundum. Pin et al. (2006) suggested that the corundum-bearing albitite dikes in the western Pyrenees (France) are products of very-low-degree (<1%) partial melting of a harzburgite source previously enriched by carbonatite-related metasomatism and that volatile components (H_2O and CO_2) may account for the crystallization of corundum by controlling the solubility of Al_2O_3 and SiO_2 in mantle fluids.

Aspen et al. (1990) described corundum megacrysts associated with anorthoclase and sanidine found in alkali basalt in Scotland and considered that corundum originated from the crystallization of syenite generated in the crust or the upper mantle. Guo et al. (1996) proposed that corundum crystallized from interactions and hybridization between carbonatitic and pegmatitic liquids and was uplifted to the surface during subsequent rifting and igneous activity.

Rocks from the mantle and the crust have distinct oxygen isotope compositions, thus the $\delta^{18}O$ of corundum can explain the source origin of corundum-bearing rocks (Yui et al. 2003, 2006; Giuliani et al. 2005, 2009; Vysotskiy et al. 2015). The oxygen isotope values of six corundum samples from the Yushishan syenite range from 6.2‰ to 8.2‰ and overlap with the range for sapphires associated with syenites ($4.4 < \delta^{18}O < 8.3$‰, mean $\delta^{18}O = 6.8 \pm 1.4$‰, n = 29; Giuliani et al. 2009) (Fig. 11). The oxygen isotope range of corundum in the Yushishan area is the same as that of corundum (sapphire) from syenite in Ontario (Canadian) syenite (7.6‰−9.3‰), one outlier of 8.4‰ of sapphire xenocrysts in alkali basalt from Denchai (Thailand) and sapphire in syenite from Beforona (Madagascar) (8.1‰), and is significantly higher than oxygen isotope of corundum (sapphire) in anorthoclasite from Menet (4.4‰) (French), Kianjanakanga (4.5‰) (Madagascar) and Gortva (5.1‰) (Slovakia) and in syenite pegmatite from Ilmen (3.2‰−4.4‰) (Russia) and in monzonite from Garba Tula (4.7‰-5.3‰) (Kenya), and sapphire xenocrysts in alkali basalt from Denchai (4.7‰–6.1‰) (Thailand), Changle (4.6‰–5.7‰) (China), Weldborough (5.1‰–6.2‰) and Barrington (4.6‰–5.8‰) in Australia and Dak Nong (5.0‰–5.2‰) (Vietnam). Considering that most deposits listed above have single source of corundum (sapphire), on the premise that without separating corundum oxygen isotope values from the same deposit into different groups, except for sapphire from Denchai which has a outlier of 8.4‰, these corundum deposits can be approximately divided into two groups according to oxygen isotope ranges, one group with higher $\delta^{18}O$ is 6.2‰-9.3‰ where Yushishan corundum is located (red area), while the other group with lower $\delta^{18}O$ of 3.2‰-6.2‰ (yellow area) (Fig. 11). Previous studies suggest that crystallized corundum originates from the low-degree partial melting (1%) of mantle rock and present $\delta^{18}O$ values of corundum between 5‰ and 6‰ (Yui et al. 2003). Moreover, deep-sourced parent magma can be further contaminated with crustal material during later evolution, which can be reflected in the variations of corundum oxygen isotopes ($4.8 < \delta^{18}O < 8.4$‰; Yui et al. 2003, 2006; Giuliani et al. 2005,2007). For the group with lower $\delta^{18}O$, previous studies display that corundum commonly has a mantle magmatic origin, corundum (sapphire) can crystallize from evolved melts, low volume melting of metasomatized mantle and by hybrid interactions of carbonatitic melts with silicic crustal (e.g., Irving 1986; Guo et al. 1996; Sutherland et al. 1998; Upton et al. 1999). Crustal contamination during the process was minimal. For the group with higher $\delta^{18}O$, two possible mechanisms may account for the high oxygen isotope. (1) Corundum crystallized in melt from partial melting of alumina-rich crustal materials that has been reported by Raith et al. (2010) and Li et al. (2020). In their studies, the peritectic corundum was formed by dehydration melting of muscovite through two successive reactions: muscovite → corundum + K-feldspar + liquid, and muscovite + aluminosilicate → corundum + liquid (Raith et al. 2010). Palke et al. (2016) also suggested that corundum (sapphire) from Yogo lamprophyre dike could have been produced through peritectic melting of kyanite leaving a solid residue of corundum, plagioclase, pyroxene, and garnet as well as a silicate liquid. In the mechanism of peritectic origin, the higher $\delta^{18}O$ (6.2‰-9.3‰) range of corundum can be explained by the $\delta^{18}O$ range of crustal materials, which is given by Kempton and Harmon (1992) from lower crustal xenoliths. However, the petrological and mineralogical observations described before (Fig. 3 and Fig. 4) seemingly don't favor this mechanism. (2) In this mechanism, crustal contamination was considered. Corundum might have crystallized from evolved mantle melts assimilating lower/mid-crust high $\delta^{18}O$ rocks through the process of assimilation–fractionation–crystallization (Yui et al. 2003). The chemical nature of the contaminants need be considered to satisfy the corundum crystallization environments of alumina-oversaturation and silica-poor for the final melt (Simonet et al. 2008; Giuliani et al. 2014a). Candidate rocks with these characteristics include the remnants of weathering or paleosols and aluminum-rich residues formed by the partial melting of metapelites (Levinson and Cook 1994; Osanai et al. 1998; Frings and Buss 2019; Li et al. 2020). This mechanism is more likely the source of Yushishan corundum-bearing syenite. However, although the involvement of crustal material in the formation of corundum is sure, the detailed geological process and source of corundum-bearing syenite is still not clear. A whole rock quantitative analysis for the syenite and geochronology on mineral inclusions such as zircon are needed in the future.

IMPLICATIONS

The corundum-bearing syenites are relatively rare, and only a few in-situ corundum-bearing igneous species are described in previous studies. This study reports corundum-bearing syenite in detail for the first time in the Yushishan area in the eastern part of the Altyn Tagh fault. Petrographic, mineralogical, and elemental geochemical analyses reveal the magmatic genesis of the corundum. Scanning electron microscopy (SEM) and optical microscope observations were used to identify two groups of mineral inclusions within the corundum crystals. The primary mineral inclusions indicate that the corundum crystallized in a highly evolved and differentiated peraluminous Zr-rich and Si-poor alkali magma. The secondary mineral inclusions indicate that the corundum overprints fluid-infiltration activity. Additionally, we found that typical mineral inclusions (e.g., spinel) can be the metamorphic product of corundum rather than of a simultaneously or previously crystallized primary inclusion. Minerals such as ilmenite and magnetite can appear in both groups (primary and secondary mineral inclusions); But their morphological characteristics indicated different origins.

The trace elements of corundum in the Yushishan syenite are characterized by high Fe and Ga contents and low Mg content that are consistent with a magmatic origin and comparable to corundum trace elements in other regional syenites. The corundum oxygen isotope values of 6.2‰–8.2‰ suggest that the Yushishan syenite originated from melts with notable involvement of Al-rich and Si-poor crustal material. The Yushishan is a rare metal deposit that the Nb- and Ta-bearing minerals are mainly distributed in the gneiss, which suggests that the Nb-Ta mineralization may be linked to melting processes. Although the genetic relationship between the Nb-Ta mineralization and syenite is not clear yet, the presence of mineral inclusions with Nb and Ta (columbite-(Fe), samarskite-(Y)) during crystallization revealed from corundum suggests these melting and fluid infiltration processes may change the physic-chemical factors and lead to Nb and Ta precipitation in the gneiss.

ACKNOWLEDGMENTS

This work was financially supported by the National Key Research and Development Program (Grant no. 2017YFC0602401), and National Natural Science Foundations of China (Grant no. 41972220) and Excellent Youth Fund of National Natural Science Foundation of China (Grant no. 41722207).

REFERENCES CITED

Agangi, A., Kamenetsky, V.S., and McPhie, J. (2010) The role of fluorine in the concentration and transport of lithophile trace elements in felsic magmas: Insights from the Gawler Range Volcanics, South Australia. Chemical Geology, 273(3), 314-325.

Aspen, P., Upton, B.G.J., and Dickin, A.P. (1990) Anorthoclase, sanidine and associated megacrysts in scottish alkali basalts - high-pressure syenitic debris from upper mantle sources. European Journal of Mineralogy, 2(4), 503-517.

Baldwin, L.C., Tomaschek, F., Ballhaus, C., Gerdes, A., Fonseca, R.O.C., Wirth, R., Geisler, T., and Nagel, T. (2017) Petrogenesis of alkaline basalt-hosted sapphire megacrysts. Petrological and geochemical investigations of in situ sapphire occurrences from the Siebengebirge Volcanic Field, Germany. Contributions to Mineralogy and Petrology, 172(6),43.

Cartwright, I., and Barnicoat, A.C. (1986) The generation of quartz-normative melts and corundum-bearing restites by crustal anatexis: Petrogenetic modelling based on an example from the Lewisian of North-West Scotland. Journal of Metamorphic Geology, 4(1), 79-99.

Coenraads, R. (1992) Surface features on natural rubies and sapphires derived from volcanic provinces. Journal of Gemmology, 23, 151–160.

Downes, P.J., and Bevan, A.W.R. (2002) Chrysoberyl, beryl and zincian spinel mineralization in granulite-facies Archaean rocks at Dowerin, Western Australia. Mineralogical Magazine, 66(6), 985-1002.

Dzikowski, T.J., Cempírek, J., Groat, L.A., Dipple, G.M., and Giuliani, G. (2014) Origin of gem corundum in calcite marble: the Revelstoke occurrence in the Canadian Cordillera of British Columbia. Lithos, 198-199, 281-297.

Emmett, J.L., Scarratt, K., McClure, S.F., Moses, T., Douthit, T.R., Hughes, R.,Novak, S., Shigley, J.E., Wang, W., Bordelon, O., and Kane, R.E. (2003) Beryllium diffusion of ruby and sapphires. Gems & Gemology, 39, 84–135.

Emmett, J.L., Stone-Sundberg, J., Guan, Y., and Sun, Z. (2017) The Role of Silicon in the Color of Gem Corundum. Gems & Gemology, 53(1), 42-47.

Estrade, G., Béziat, D., Salvi, S., Tiepolo, M., Paquette, J.L., and Rakotovao, S. (2014) Unusual evolution of silica-under- and -oversaturated alkaline rocks in the Cenozoic Ambohimirahavavy Complex (Madagascar): Mineralogical and geochemical evidence. Lithos, 206-207, 361-383.

Filina, M.I., Sorokina, E.S., Botcharnikov, R., Karampelas, S., Rassomakhin, M.A., Kononkova, N.N., Nikolaev, A.G., Berndt, J., and Hofmeister, W. (2019) Corundum anorthosites-kyshtymites from the South Urals, Russia: A combined mineralogical, geochemical, and U-Pb zircon geochronological study. Minerals, 9(4), 234.

Frings, P.J., and Buss, H.L. (2019) The Central Role of Weathering in the Geosciences. Elements, 15(4), 229-234.

Garnier, V., Ohnenstetter, D., Giuliani, G., Fallick, A.E., Trong, T.P., Quang, V.H., Van, L.P., and Schwarz, D. (2005) Basalt petrology, zircon ages and sapphire genesis from Dak Nong, southern Vietnam. Mineralogical Magazine, 69(1), 21-38.

Garnier, V., Giuliani, G., Ohnenstetter, D., Fallick, A.E., Dubessy, J., Banks, D., Vinh, H.Q., Lhomme, T., Maluski, H., Pêcher, A., Bakhsh, K.A., Long, P.V., Trinh, P.T., and Schwarz, D. (2008) Marble-hosted ruby deposits from Central and Southeast Asia: Towards a new genetic model. Ore Geology Reviews, 34(1), 169-191.

Giuliani, G., Fallick, A.E., Garnier, V., France-Lanord, C., Ohnenstetter, D., and Schwarz, D. (2005) Oxygen isotope composition as a tracer for the origins of rubies and sapphires. Geology, 33(4),249–252.

Giuliani, G., Fallick,A.F., Rakotondrazafy, M., Ohnenstetter, D., Andriamamonjy, A., Ralantoarison, T., Rakotosamizanany, S., Razanatseheno, M., Offant, Y., Garnier, V., Dunaigre, C., Schwarz, D., Mercier, A., Ratrimo, V., and Ralison, B. (2007) Oxygen isotope systematics of gem corundum deposits in Madagascar: relevance for their geological origin. Miner Deposita 42:251–270.

Giuliani, G., Fallick, A., Ohnenstetter, D., and Pegere, G. (2009) Oxygen isotopes composition of sapphires from the French Massif Central: Implications for the origin of gem corundum in basaltic fields. Mineralium Deposita, 44(2), 221-231.

Giuliani, G., Ohnenstetter, D., Fallick, A., Groat, L., and Fagan, A.J. (2014a) The geology and genesis of gem corundum deposits. In Geology of Gem Deposits; Groat, L.A., Ed.; Mineralogical Association of Canada: Tucson, AZ,USA, pp. 29–112.

Giuliani, G., Caumon, G., Rakotosamizanany, S., Ohnenstetter,D., and Rakototondrazafy, M. (2014b) Classification chimique des corindons par analyse factorielle discriminante:Application `a la typologie des gisements de rubis et saphirs.Revue de Gemmologie 188, 14–22.

Graham, I., Sutherland, L., Zaw, K., Nechaev, V., and Khanchuk, A. (2008) Advances in our understanding of the gem corundum deposits of the West Pacific continental margins intraplate basaltic fields. Ore Geology Reviews, 34(1-2), 200-215.

Guo, J.F., Oreilly, S.Y., and Griffin, W.L. (1996) Corundum from basaltic terrains: A mineral inclusion approach to the enigma. Contributions to Mineralogy and Petrology, 122(4), 368-386.

Hattori, K.H., Guillot, S., Saumur, B.M., Tubrett, M.N., Vidal, O., and Morfin, S. (2010) Corundum-bearing garnet peridotite from northern Dominican Republic: A metamorphic product of an arc cumulate in the Caribbean subduction zone. Lithos, 114(3-4), 437-450.

He, Z.Y., Zhang, Z.M., Zong, K.Q., and Dong, X. (2013) Paleoproterozoic crustal evolution of the Tarim Craton: Constrained by zircon U–Pb and Hf isotopes of meta-igneous rocks from Korla and Dunhuang. Journal of Asian Earth Sciences, 78(15), 54-70.

Hu, W., Song, Y., Chen, X., Tao, M., and Zhang, L. (2007) Noble gases in corundum megacrysts from the basalts in Changle, Shandong Province, eastern China. Chinese Science Bulletin, 52(3), 380-387.

Huang, H., Wang, T., Zhang, Z., Li, C., and Qin, Q. (2018) Highly differentiated fluorine-rich, alkaline granitic magma linked to rare metal mineralization: A case study from the Boziguo'er rare metal granitic pluton in South Tianshan Terrane, Xinjiang, NW China. Ore Geology Reviews, 96, 146-163.

Huang, W., Ni, P., Shui, T., Pan, J., Fan, M., Yang, Y., Chi, Z., and Ding, J. (2021) Trace element geochemistry and mineral inclusions constraints on the petrogenesis of a marble hosted ruby deposit in Yunnan Province, China. The Canadian Mineralogist, 59(2), 381-408.

Hughes, R.W. (1997) Ruby & Sapphire, PWH Publishing, Boulder, Colorado, 512 p.

Icenhower, J., and London, D. (1995) An experimental study of element partitioning among biotite, muscovite, and coexisting peraluminous silicic melt at 200 MPa (H2O). American Mineralogist, 80(11-12), 1229-1251.

Irving, A. J. (1986) Polybaric magma mixing in alkali basalts and kimberlites: Evidence from corundum, zircon and ilmenite megacrysts. The Agora Political Science Undergraduate Journal, 4(1), 262-264.

Izokh, A.E., Smirnov, S.Z., Egorova, V.V., Anh, T.T., Kovyazin, S.V., Phuong, N.T., and Kalinina, V.V. (2010) The conditions of formation of sapphire and zircon in the areas of alkali-basaltoid volcanism in Central Vietnam. Russian Geology and Geophysics, 51(7), 719-733.

Jia, Z.L., Dou,X.Y., Wang, J.R., Zhang,D., and Hou, R.N. (2016) Restoration of granulite source rocks in the Yushishan area, Nanqilian, Gansu. Gansu geology, 25(2), 9-14 (in Chinese with English abstract).

Jochum, K.P., Weis, U., Stoll, B., Kuzmin, D., Yang, Q., Raczek, I., Jacob, D.E., Stracke, A., Birbaum, K., Frick, D.A., Günther, D., and Enzweiler, J. (2011) Determination of referencevalues for NIST SRM 610-617 glasses following ISO guidelines. Geostandards & Geoanalytical Research, 35, 397–429.

Kan-Nyunt, H.-P., Karampelas, S., Link, K., Thu, K., Kiefert, L., and Hardy, P. (2013) Blue sapphires from the Baw Mar Mine in Mogok. Gems & Gemology 49(4),223–232.

Keller, D.S., and Ague, J.J. (2018) High-pressure granulite facies metamorphism (~1.8 GPa) revealed in silica-undersaturated garnet-spinel-corundum gneiss, Central Maine Terrane, Connecticut, U.S.A. American Mineralogist, 103(11), 1851-1868.

Kerrich, R., Fyfe, W.S., Barnett, R.L., Blair, B.B., and Willmore, L.M. (1987) Corundum, Cr-muscovite rocks at O'Briens, Zimbabwe: The conjunctionof hydrothermal desilicification and LIL-element enrichment—Geochemical and isotope evidence: Contributions to Mineralogy and Petrology, 95, 481–498,

Kempton, P.D., and Harmon, R.S. (1992) Oxygen isotope evidence for large-scale hybridization of the lower continental crust during magmatic underplating. Geochimica et Cosmochimica Acta, 56, 971–986.

Khamloet, P., Pisutha-Arnond, V., and Sutthirat, C. (2014) Mineral inclusions in sapphire from the basalt-related deposit in Bo Phloi, Kanchanaburi, western Thailand: indication of their genesis. Russian Geology and Geophysics, 55(9), 1087-1102.

Kievlenko, E.Y. (2003) Geology of Gems. Ocean Pictures Ltd, Littleton, CO, USA.

Kong, F.M., Li, X. P., Zhao, L, Q., Chen, S., and Yin, Q. H. (2017) Petrography and mineral chemistry of corundum and spinel menocryst in the Cenozoic Basalt at Changle, Shandong Prinvice. Geological Review, 63(2), 441-457 (in Chinese with English abstract).

Levinson, A.A., and Cook, F.A. (1994) Gem corundum in alkali basalt: origin and occurrence. Gems & Gemology 30, 253– 262.

Li, Y., Yang, Y., Liu, Y.C., Groppo, C., and Rolfo, F. (2020) Muscovite dehydration melting in silica-undersaturated systems: A case study from corundum-bearing anatectic rocks in the Dabie Orogen. Minerals, 10(3), 213.

Li, X.W., Cao, S.Y., Liu, J.H., Zhou, D.K., Li, W,X., Jiang,S.Y., Cao, H.C., and Wu, Y. (2021) Geological structure characteristics and fluid activity of the gold-bearing quartz veins on the Yushishan area, North Altyn Tagh. Geotectonica et Metallogenia. In press (in Chinese with English abstract).

Liu,L., Che, Z.C., Wang,Y., Luo, J.H. and Chen,D.L. (1999) The petrological characters and geotectonic setting of high-pressure metamorphic rock belts in Altun Mountains. Acta Petrologica Sinica, 15(1), 57- 64 (in Chinese with English abstract).

Liu, Y.J., Neubauer, F., Genser, J., Ge, X.-H., Takasu, A., Yuan, S.H., Chang, L.H., and Li, W.M. (2007) Geochronology of the initiation and displacement of the Altyn Strike-Slip Fault, western China. Journal of Asian Earth Sciences, 29(2), 243-252.

Liu, Y.S., Hu, Z.C., Gao, S., Günther, D., Xu, J., Gao, C.G. and Chen, H.H. (2008) In situ analysis of major and trace elements of anhydrous minerals by LA-ICP-MS without applying an internal standard. Chemical Geology, 257(1-2), 34-43.

Lu, S.N., Li, H.K., Zhang, C.L., and Niu, G. H. (2008) Geological and geochronological evidence for the Precambrian evolution of the Tarim craton and surrounding continental fragments. Precambrian Research, 160, 94-107.

McGee, B.M. (2005) Characteristics and origin of the Weldborough sapphire, NE Tasmania, B.Sc. thesis, University of Tasmania, Hobart. 118 p.

Mazzone, P., and Stephen, E. H. (1989) Peraluminous xenoliths in kimberlite: Metamorphosed restites produced by partial melting of pelites. Geochimica et Cosmochimica Acta, 53(7), 1551-1561.

Meng, F., Shmelev, V.R., Kulikova, K.V., and Ren, Y. (2018) A red-corundum-bearing vein in the Rai–Iz ultramafic rocks, Polar Urals, Russia: the product of fluid activity in a subduction zone. Lithos, 320-321, 302-314.

Monchoux, P., Fontan, F., De Parseval, P., Martin, R.F., and Wang, R.C. (2006) Igneous albitite dikes in orogenic lherzolites, western Pyrenees, France: A possible source for corundum and alkali feldspar xenocrysts in basaltic terranes. I. Mineralogical associations. Canadian Mineralogist, 44, 817-842.

Moon, A.R., and Phillips, M.R. (1984) An electron microscopy study of exsolved phases in natural black Australian sapphire. Micron and Microscopica Acta, 15(3), 143-146.

Moyd, L. (1949) Petrology of the nepheline andcorundum rocks of southeastern Ontario. American Mineralogist, 34, 736–751.

Osanai, Y., Hamamoto, T., Maishima, O., and Kagami, H. (1998) Sapphirine- bearing granulites and related high-temperature metamorphic rocks from the Higo metamorphic terrane, west-central Kyushu, Japan. Journal of Metamorphic Geology, 16, 53–66.

Pakhomova, V.A., Zalishchak, B.L., Odarichenko, E.G., Lapina, M.I., and Karmanov, N.S. (2006) Study of melt inclusions in the Nezametnoye corundum deposit, Primorsky region of the Russian Far East: Petrogenetic consequences. Journal of Geochemical Exploration, 89(1), 302-305.

Palke, A.C., Renfro, N.D., and Berg, R.B. (2016) Origin of sapphires from a lamprophyre dike at Yogo Gulch, Montana, USA: Clues from their melt inclusions. Lithos, 260, 339-344.

Palke, A.C., and Breeding, C.M. (2017) The origin of needle-like rutile inclusions in natural gem corundum: A combined EPMA, LA-ICP-MS, and nanoSIMS investigation. American Mineralogist, 102(7), 1451-1461.

Palke, A.C., Renfro, N.D., and Berg, R.B. (2017) Melt inclusions in alluvial sapphires from Montana, USA: Formation of sapphires as a restitic component of lower crustal melting? Lithos, 278-281, 43-53.

Peretti, A., Peretti, F., Kanpraphai, A., Bieri,W., Hametner, C. and Günther, D. (2008) Winza rubies identified. Contributions to Gemology, 7, 1–97.

DOI: https://doi.org/10.2138/am-2022-8223. http://www.minsocam.org/

Peucat, J.J., Ruffault, P., Fritsch, E., Bouhnik-Le Coz, M., Simonet, C., and Lasnier, B. (2007) Ga/Mg ratio as a new geochemical tool to differentiate magmatic from metamorphic blue sapphires. Lithos, 98(1-4), 261-274.

Pham, V.T., Wang, H., Zhang, Q., Liu, J.H., Shi, M.Y., Li, Z., and Wu, C.M. (2018) Metamorphic evolution and geochronology of the Changshanzi area, Dunhuang Orogenic Belt, Northwest China. Acta Petrologica Sinica, 34, 2773-2792 (in Chinese with English abstract).

Pin, C., Monchoux, P., Paquette, J.L., Azambre, B., Wang, R.C., and Martin, R.F. (2006) Igneous albitite dikes in orogenic lherzolites, western Pyrenees, France: A possible source for corundum and alkali feldspar xenocrysts in basaltic terranes. II. Geochemical and petrogenetic considerations. Canadian Mineralogist, 44, 843-856.

Raith, M.M., Rakotondrazafy, R., and Sengupta, P. (2010) Petrology of corundum-spinel-sapphirine-anorthite rocks (sakenites) from the type locality in southern Madagascar. Journal of Metamorphic Geology, 26(6), 647-667.

Rakotondrazafy, A.F.M., Giuliani, G., Ohnenstetter, D., Fallick, A.E., Rakotosamizanany, S., Andriamamonjy, A., Ralantoarison, T., Razanatseheno, M., Offant, Y., Garnier,V.,Maluski, H., Dunaigre, C., Schwarz, D., and Ratrimo, V. (2008) Gem corundum deposits of Madagascar: A review. Ore Geology Reviews, 34(1-2), 134-154.

Rakotosamizanany, S., Giuliani, G., Ohnenstetter, D., Rakotondrazafy, A.F.M., Fallick, A.E., Paquette, J.L., and Tiepolo, M. (2014) Chemical and oxygen isotopic compositions, age and origin of gem corundums in Madagascar alkali basalts. Journal of African Earth Sciences, 94, 156-170.

Riesco, M., Stüwe, K., and Reche, J. (2005) Formation of corundum in metapelites around ultramafic bodies. An example from the Saualpe region, Eastern Alps. Mineralogy and Petrology, 83(1-2), 1-25.

Rossman, G.R. (2009) The geochemistry of gems and its relevance to gemology: Different traces, different prices. Elements, 5, 159–162.

Schwarz, D., Pardieu, V., Saul, J.M., Schmetzer, K., Laurs, B.M., Giuliani, G., Klemm, L., Malsy, A.K., Hauzenberger, C., Du Toit, G., Fallick, A.E., and Ohnenstetter, D. (2008) Ruby and sapphires from Winza (Central Tanzania). Gems & Gemology, 44, 322–347.

Simonet, C., Paquette, J.L., Pin, C., Lasnier, B., and Fritsch, E. (2004) The Dusi (Garba Tula) sapphire deposit, Central Kenya—A unique Pan-African corundum-bearing monzonite. Journal of African Earth Sciences, 38(4), 401-410.

Simonet, C., Fritsch, E., and Lasnier, B. (2008) A classification of gem corundum deposits aimed towards gem exploration. Ore Geology Reviews, 34(1-2), 127-133.

Song, Y. C, and Hu, W, X. (2009) Carbonates and sulfates-bearing melt inclusions in corundum megacrysts from Changle basalts of Shandong province and their implications. Acta Petrol Miner 28, 349–363 (in Chinese with English abstract).

Soonthorntantikul, W., Vertriest, W., Raynaud-Flattot, V.L., Sangsawong, S., Atikarnsakul, U., Khowpong, CH., Weeramonkhonlert, V., and Pardieu, V. (2017) An indepth gemological study of blue sapphires from the Baw Mar mine (Mogok, Myanmar). Gemmological Institute of America Report, 87 pp.

Sorokina, E.S., Hofmeister, W., Häger, T., Mertz-Kraus, R., Buhre, S., and Saul, J.M. (2016) Morphological and chemical evolution of corundum (ruby and sapphire): Crystal ontogeny reconstructed by EMPA, LA-ICP-MS, and Cr^{3+} Raman mapping. American Mineralogist, 101(12), 2716–2722.

Sorokina, E.S., Karampelas, S., Nishanbaev, T.P., Nikandrov, S.N., and Semiannikov, B.S. (2017) Sapphire megacrysts in syenite pegmatites from the Ilmen Mountains, South Urals, Russia: New mineralogical data. The Canadian Mineralogist, 55(5), 823-843.

Sorokina, E., Rassomakhin, M., Nikandrov, S., Karampelas, S., Kononkova, N., Nikolaev, A., Anosova, M., Somsikova, A., Kostitsyn, Y., and Kotlyarov, V. (2019) Origin of Blue Sapphire in Newly Discovered Spinel–Chlorite–Muscovite Rocks within Meta-Ultramafites of Ilmen Mountains, South Urals of Russia: Evidence from Mineralogy, Geochemistry, Rb-Sr and Sm-Nd Isotopic Data. Minerals, 9(1).

Sorokina, E.S., Botcharnikov, R.E., Kostitsyn, Y.A., Rösel, D., Häger, T., Rassomakhin, M.A., Kononkova, N.N., Somsikova, A.V., Berndt, J., Ludwig, T., Medvedeva, E.V., and Hofmeister, W. (2021) Sapphire-bearing magmatic rocks trace the boundary between paleo-continents: A case study of Ilmenogorsky alkaline complex, Uralian collision zone of Russia. Gondwana Research, 92, 239-252.

Stern, R.J., Tsujimori, T., Harlow, G., and Groat, L.A. (2013) Plate tectonic gemstones. Geology, 41(7), 723-726.

Sutherland, F.L., Hoskin, P.W.O., Fanning, C.M., and Coenraads, R.R. (1998) Models of corundum origin from alkali basaltic terrains: A reappraisal. Contributions to Mineralogy and Petrology, 133(4), 356-372.

Sutherland, F.L., Duroc-Danner, J.M., and Meffre, S. (2008) Age and origin of gem corundum and zircon megacrysts from the Mercaderes–Rio Mayo area, South-west Colombia, South America. Ore Geology Reviews, 34(1-2), 155-168.

Sutherland, F.L., Zaw, K., Meffre, S., Giuliani, G., Fallick, A.E., Graham, I.T., and Webb, G.B. (2009) Gem-corundum megacrysts from east Australian basalt fields: Trace elements, oxygen isotopes and origins. Australian Journal of Earth Sciences. 56 (7), 1003–1022.

Sutherland, F.L., Coenraads, R.R., Abduriyim, A., Meffre, S., Hoskin, P.W.O., Giuliani, G.,Beattie, R., Wuhrer, R., and Sutherland, G.B. (2015) Corundum (sapphire) and zircon relationships, Lava Plains gem fields, NE Australia: Integrated mineralogy, geochemistry, age determination, genesis and geographical typing. Mineralogical Magazine, 79, 545–581.

Uher, P., Giuliani, G., Szakáll, S., Fallick, A., Strunga, V., Vaculovič, T., Ozdín, D., and Gregáňová, M. (2012) Sapphires related to alkali basalts from the Cerová Highlands, Western Carpathians (southern Slovakia): Composition and origin. Geologica Carpathica, 63(1), 71-82.

Upton, B.G.J., Hinton, R.W., Aspen, P., Finch,A.A., and Valley, J.W. (1999) Megacrysts and associated xenoliths: Evidence for migration of geochemically enriched melts in the upper mantle beneath Scotland. Journal of Petrology, 40, 935–956.

Vysotskiy, S.V., Nechaev, V.P., Kissin, A.Y., Yakovlenko, V.V., Velivetskaya, T.A., Sutherland,F.L., and Agoshkov, A.I. (2015) Oxygen isotopic composition as an indicator of ruby and sapphire origin: A review of Russian occurrences. Ore Geology Reviews, 68, 164–170.

Wang, J., Li, X.Q., Liang, M.H., Wang, Y.X., Zhang, B.B., and Pan, B.T. (2018) Age and geochemistry of Aksay ophiolite in East Altun Mountains. Geological Bulletin of China, 37(4), 559-569.

Wu, C.L., Yang, J.S., Robinson, P.T., Wooden, J.L., Mazdab, F.K., Gao, Y.H., Wu, S.P., and Chen, Q.L. (2009) Geochemistry, age and tectonic significance of granitic rocks in north Altun, northwest China. Lithos, 113(3), 423-436.

Yakymchuk, C., and Szilas, K. (2017) Corundum formation by metasomatic reactions in Archean metapelite, SW Greenland: Exploration vectors for ruby deposits within high-grade greenstone belts. Geoscience Frontiers, 9(3), 727-749.

Yang, J. S., Shi, R. D., Wu, C. L., Shu, D. C., Chen, S. Y., Wang, X. B., Wooden, J. (2008) Petrology and SHRIMP age of the Hongliugou ophiolite at Milan, north Altun, at the northern margin of the Tibetan plateau. Acta Petrologica Sinica, 24(7), 1567-1584 (in Chinese with English abstract).

Yu, J.P., Wu, Y.B., Liang, M.H., Xiao, P.X., and Dou, X.Y. (2015) New progress of the southern Altyn Tagh geological mapping and guide the prospecting support: According to 1:50000 Mobeier and other five regional geological maps in Gansu Province. Geological Survey of China, 2, 40–47 (in Chinese with English abstract).

Yui, T.F., Khin, Z., and Limtrakun, P. (2003) Oxygen isotope composition of the Denchai sapphire, Thailand: A clue to its enigmatic origin. Lithos, 67(1-2), 153-161.

Yui, T.F., Wu, C.M., Limtrakun, P., Sricharn, W., and Boonsoong, A. (2006) Oxygen isotope studies on placer sapphire and ruby in the Chanthaburi-Trat alkali basaltic gemfield, Thailand. Lithos, 86(3-4), 197-211.

Zaw, K., Sutherland, F.L., Dellapasqua, F., Ryan, C.G., Yui, T.F., Mernagh, T.P., and Duncan, D. (2006) Contrasts in gem corundum characteristics, eastern Australian basaltic fields: Trace elements, fluid/melt inclusions and oxygen isotopes. Mineralogical Magazine, 70(6), 669-687.

Zhang, J.X., Yu, S.Y., Gong, J.H., Li, H.K., and Hou, K.J. (2013) The latest Neoarchean–Paleoproterozoic evolution of the Dunhuang block, eastern Tarim craton, northwestern China: Evidence from zircon U–Pb dating and Hf isotopic analyses. Precambrian Research, 226, 21-42.

Zhang, J.X., Yu, S.Y., Li, Y.S., Yu, X.X., Lin, Y.H., and Mao, X.H. (2015) Subduction, accretion and closure of Proto-Tethyan Ocean: Early Paleozoic accretion/collision orogeny in the Altun-Qilian-North Qaidam orogenic system. Acta Petrologica Sinica, 31(12), 3531–3554 (in Chinese with English abstract).

Zhang, Z., Ding, H., Dong, X., Tian, Z., Mu, H., Li, M., Qin, S., Niu, Z., and Zhang, N. (2018) The Eocene corundum-bearing rocks in the Gangdese arc, south Tibet: Implications for tectonic evolution of the Himalayan orogen. Geoscience Frontiers, 9(5), 1337-1354.

Zhao, Y., Sun, Y., Diwu, C.R., Guo, A.L., Ao, W.H., and Zhu, T. (2016) The Dunhuang block is a Paleozoic orogenic belt and part of the Central Asian Orogenic Belt (CAOB), NW China. Gondwana Research, 30, 207-223.

Zhao, Y., and Sun, Y. (2018) Composition and evolution of Precambrian geological units in the composite Dunhuang orogenic belt, Northwest China. Acta Petrologica Sinica, 34, 963-980 (in Chinese with English abstract).

Zhu, Y.X., Wang, L.X., Ma, C.Q., Wiedenbeck, M., and Wang, W. (2020) The Neoproterozoic alkaline rocks from Fangcheng area, East Qinling (China) and their implications for regional Nb mineralization and tectonic evolution. Precambrian Research, 350, 105852.

Zong, K.Q., Zhang, Z.M., He, Z.Y., Hu, Z.C., Santosh, M., Liu, Y.S., and Wang, W. (2012) Early Palaeozoic high-pressure granulites from the Dunhuang block, northeastern Tarim Craton: Constraints on continental collision in the southern Central Asian Orogenic Belt. Journal of Metamorphic Geology, 30, 753-768.

Zong, K.Q., Liu, Y.S., Zhang, Z.M., He, Z.Y., Hu, Z.C., Guo, J.L., and Chen, K. (2013) The generation and evolution of Archean continental crust in the Dunhuang block, northeastern Tarim craton, northwestern China. Precambrian Research, 235, 251-263.

Zwaan, J., Buter, E., Mertz-Kraus, R., and Kane, R.E. (2015) The origin of Montana's alluvial sapphires. Gems and Gemology, 51(4).

TABLE 1. Trace element concentrations (μg/g) in corundum samples from Yushishan

Sample	Mg	Ti	V	Cr	Mn	Fe	Ga	Ga/Mg	Ga*/Al	Fe/Ti	Fe/Mg	Cr/Ga
YS1838-15	1.6	18	0.31	b.d.l	2.50	8508	181	113	3.5	475	5303	-
	7.4	101	0.27	7.3	6.95	9693	170	23	3.3	96	1306	0.043
	8.7	418	0.30	2.9	8.81	10876	184	21	3.5	26	1249	0.016
	1.8	256	0.11	5.9	1.82	10338	176	100	3.4	40	5841	0.034
	1.9	123	0.24	6.2	4.93	10041	171	92	3.3	82	5384	0.036
	11.1	117	b.d.l	3.2	2.54	10237	173	16	3.3	88	923	0.018
YS1838-16	15.3	501	0.15	2.3	9.38	10739	180	12	3.5	21	703	0.013
	18.0	771	0.26	2.7	18.53	11627	183	10	3.5	15	647	0.015
	b.d.l	23	0.05	b.d.l	b.d.l	9242	169	-	3.2	402	-	-
	1.0	72	0.36	2.0	2.87	8938	174	168	3.3	125	8621	0.012
	2.1	9	0.05	5.0	0.25	8652	185	86	3.5	984	4036	0.027
YS1834-6	13.4	25	0.39	3.3	1.74	9133	190	14	3.7	367	684	0.017
	7.4	22	0.05	5.7	1.79	9347	195	26	3.8	424	1267	0.029
	10.0	34	0.19	b.d.l	b.d.l	9211	198	20	3.8	272	921	-
YS43-12A	10.6	27	0.35	0.3	b.d.l	10037	212	20	4.1	379	949	0.002
	3.2	15	0.30	b.d.l	b.d.l	9016	178	55	3.4	599	2775	-
	10.4	19	0.41	b.d.l	b.d.l	8411	201	19	3.9	433	806	-
YS1843-13	11.7	25	0.52	b.d.l	1.11	9290	161	14	3.1	374	792	-
YS1843-14	3.8	25	1.13	0.9	b.d.l	9203	170	45	3.3	375	2454	0.005
Average	7.7	137	0.30	3.7	4.52	9607	182	47	3.5	293	2481	0.021
Detection limits (μg/g)	0.2	0.6	≤0.1	0.3	≤0.1	4.0	≤0.1					

882 **TABLE 2**. Oxygen isotope values of corundum (sapphire) in syenite, monzonite and
883 anorthoclasite, and sapphire xenocrysts in alkali basalt from major regions of the world, and
884 including oxygen isotopes of corundum in the Yushishan syenite in this study.

Country	Region or mine	Colour	δ18O(‰) (V-SMOW)	Reference
		Sapphires in syenite		
China	Yushishan	grey	6.2	this work
	Yushishan	grey	6.2	this work
	Yushishan	grey	6.4	this work
	Yushishan	grey	7.1	this work
	Yushishan	light blue	7.5	this work
	Yushishan	light blue	8.2	this work
Canada	Carigmont	blue to grey	7.6	Giuliani et al. 2009
(Ontario)	Hastings-New Carlow	yellow to colorless	7.8	Giuliani et al. 2009
	Craig Hill	grey to yellow	7.6	Giuliani et al. 2009
	Dugannon	grey	9.3	Giuliani et al. 2009
	Grenville	deep blue to black	7.5	Kerrich et al. 1987
Russia	Ilmen	brown to blue	3.2	Sorokina et al. 2021
(Urals)	Ilmen	brown to blue	3.5	Sorokina et al. 2021
	Ilmen	brown to blue	4.4	Sorokina et al. 2021
Madagascar	Beforona	pink	8.1	Giuliani et al. 2007
		Sapphires in monzonite		
Kenya	Garba Tula	brown	4.7	Upton et al. 1999
		brown	4.8	Upton et al. 1999
		brown	5.3	Upton et al. 1999
		Sapphires in anorthoclasite		
French	Menet	blue	4.4	Giuliani et al. 2009
Madagascar	Kianjanakanga	deep blue	4.5	Rakotosamizanany et al. 2014
Slovakia	Gortva	blue	5.1	Uher et al. 2012
		Sapphire xenocrysts in alkali basalt		
Thailand	Denchai	dark blue	4.7	Yui et al. 2003
		blue	6.1	Yui et al. 2003
		blue-green-yellow	8.4	Yui et al. 2003
China	Changle	unknown	4.6	Hu et al. 2007
		unknown	5.2	Hu et al. 2007
		unknown	5.7	Hu et al. 2007
Australia	Weldborough	blue	5.1	Zaw et al. 2006
		blue	6.2	Zaw et al. 2006
	Barrington	black	4.6	Zaw et al. 2006
		yellow	5.8	Zaw et al. 2006
Vietnam	Dak Nong	unknown	5.0	Garnier et al. 2005

	unknown	5.2	Garnier et al. 2005

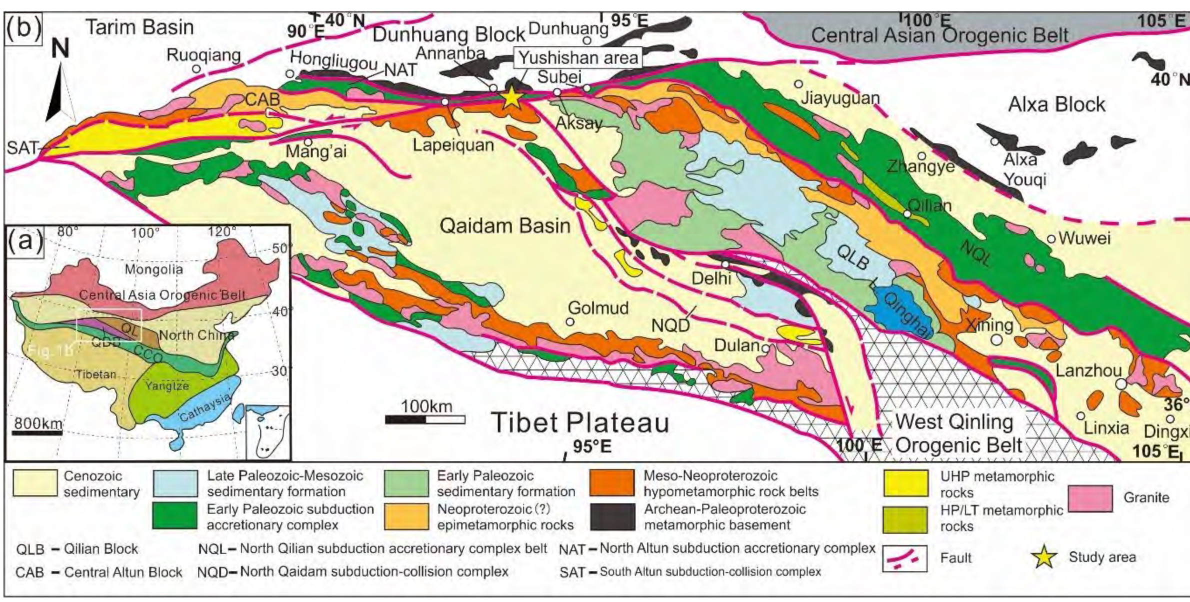

FIGURE 1. (a) Tectonic framework of China, showing the location of the Qilian block (modified from Li et al. 2012); (b) Geologic map of the Qilian block and the location of Yushishan rare metal deposits (modified from Zhang et al. 2015)

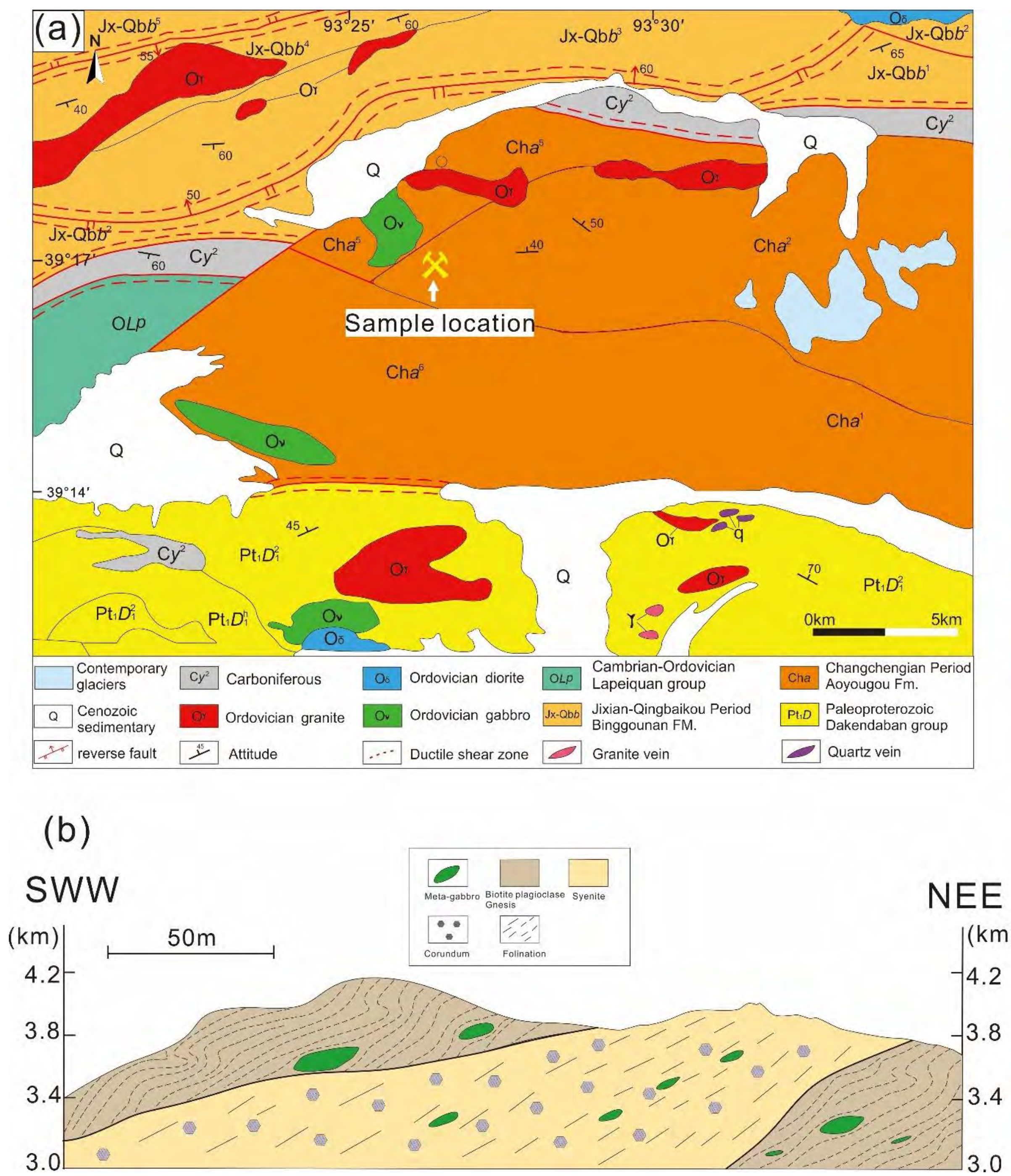

FIGURE 2. (a) Geological sketch of Yushishan deposits (from Jia et al. 2016); (b) SWW-NEE cross section across the corundum-bearing syenite outcrop.

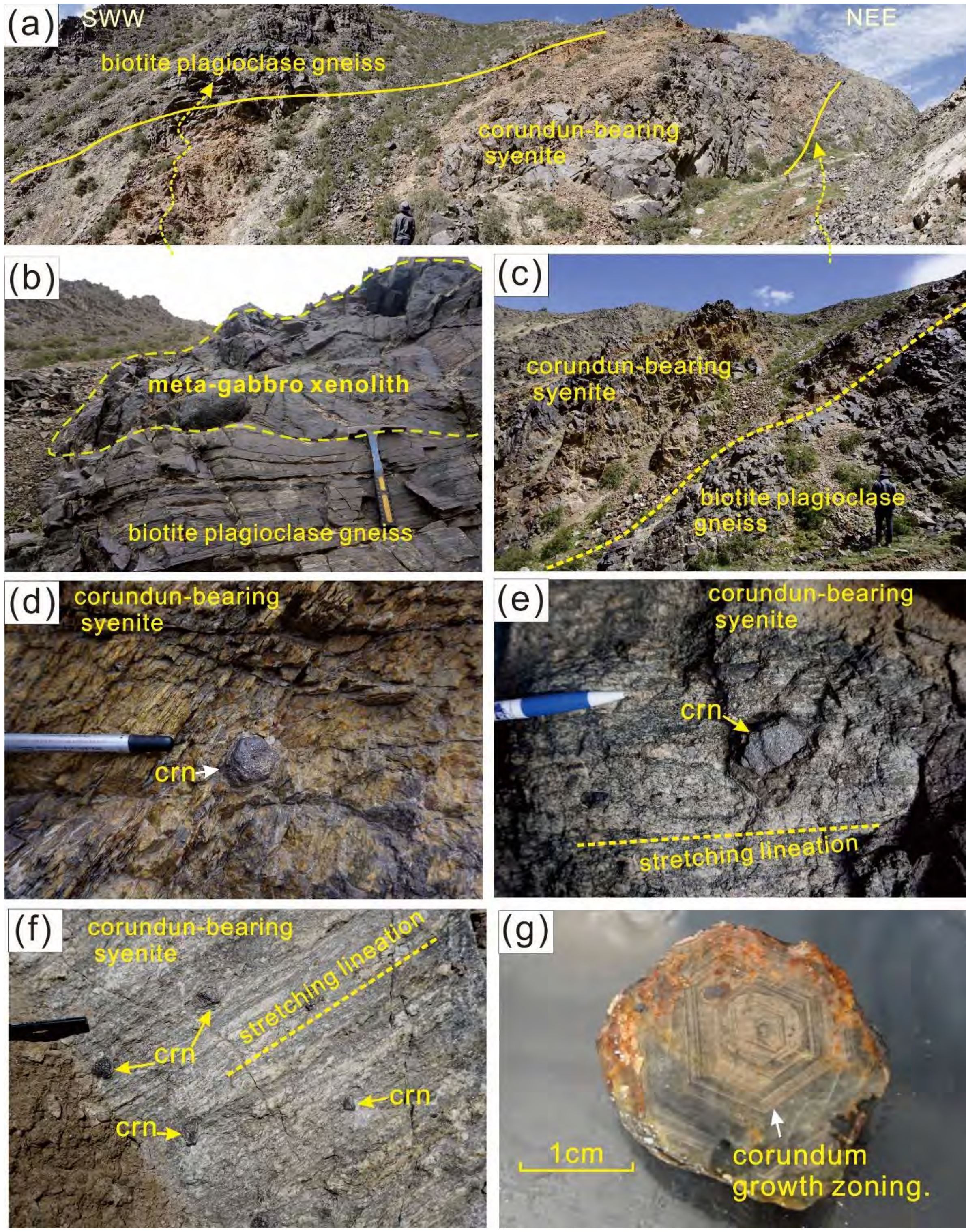

FIGURE 3. Field photographs of corundum-bearing syenite and host-rocks. (a) Overall characteristic of exposed outcrop; (b) Lens-shaped meta-gabbro xenolith; (c) Field relationship between corundum-bearing syenite and host-rock biotite plagioclase gneiss; (d) Corundum crystals are euhedral and show hexagonal prismatic habits; (e-f) Corundum porphyroclasts are rotated and the stretching lineation in syenite are well developed; (g) Single coarse-grained corundum crystal with hexagonal growth zoning in the cross-section of the corundum. Abbreviations: crn = corundum.

FIGURE 5. Photomicrographs of inclusions found in the Yushishan corundum using transmitted and reflected light on thin sections, and element distribution of needle-like Fe-Ti oxides (e-f). (a) Coarse-grained corundum with core and margin characteristics; (b) Low-density distribution of Fe-Ti oxide needles in the margin of corundum; (c) High-density distribution of Fe-Ti oxide needles in the core of corundum; (d) Inhomogeneous distribution of Fe-Ti oxide needles; (e) Ti element distribution image; (f) Fe element distribution image; (g) Irregular green Zn-rich hercynite in corundum; (h) Very fine-grained zircon with prismatic habits; (i) Brown pyrochlore as well as opaque magnetite mineral inclusions; (j) K-feldspar mineral inclusions; (k) Pyrite with secondary goethite surrounded; (l) Prismatic samarskite-(Y) mineral inclusions. Abbreviations: kfs = k-feldspar; pl = plagioclase; crn = corundum; ms = muscovite; mag = magnetite; pcl = pyrochlore; py = pyrite; gth = goethite; zrn = zircon; smk-Y = samarskite-(Y); pth = perthite.

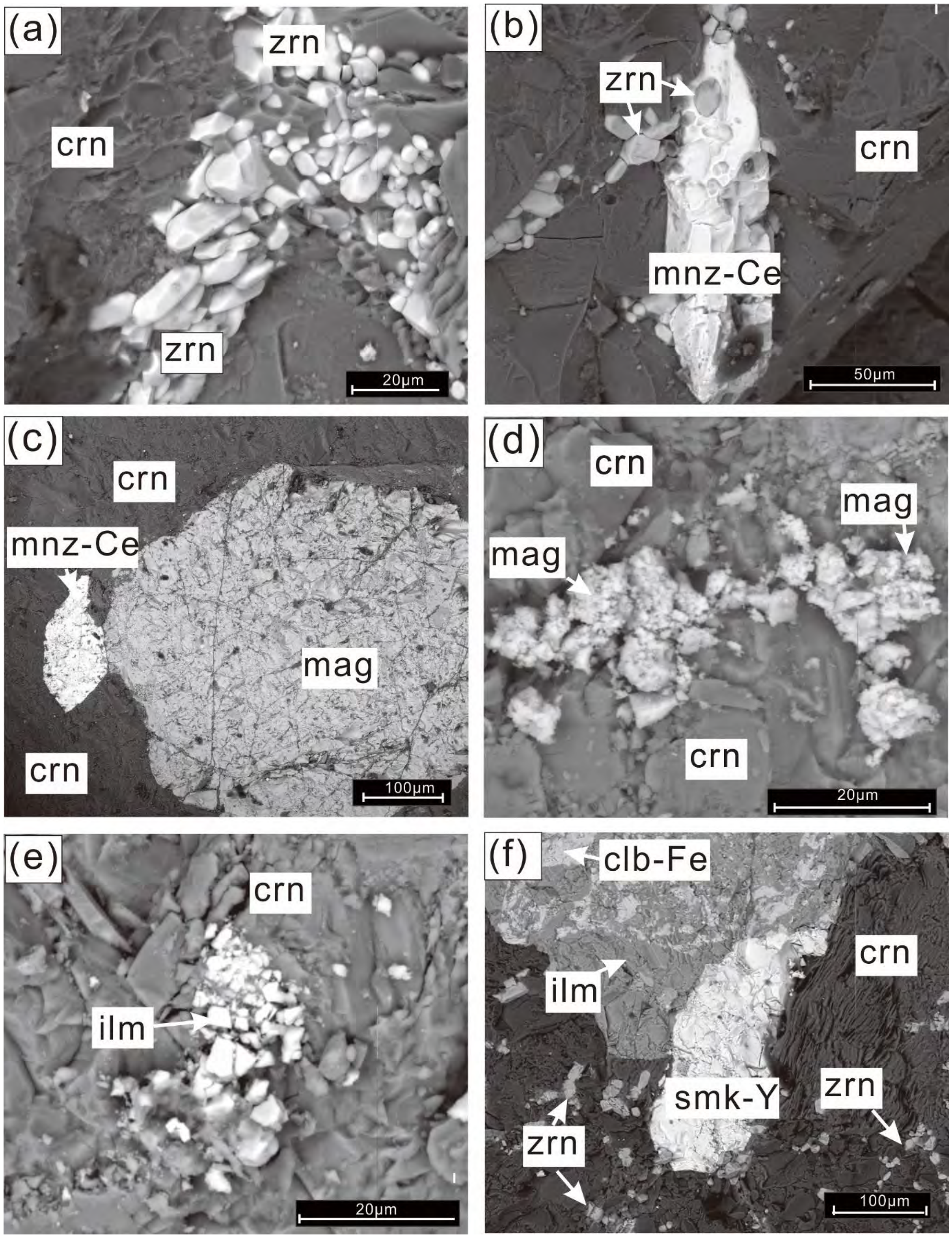

FIGURE 6. Back scattered electron images (BSE) showing primary mineral inclusions in Yushishan corundum. (a) Very fine-grained euhedral zircon aggregates; (b) Prismatic monazite-(Ce) with zircon grains inserted in; (c) Coarse-grained granular magnetite with fracture development; (d) Fine-grained magnetite; (e) Fine-grained rhombic ilmenite; (f) Prismatic samarskite-(Y). Abbreviations: crn = corundum; mnz-Ce = monazite-(Ce); zrn = zircon; ilm = ilmenite; smk-Y = samarskite-(Y); clb-Fe = columbite-(Fe); mag = magnetite.

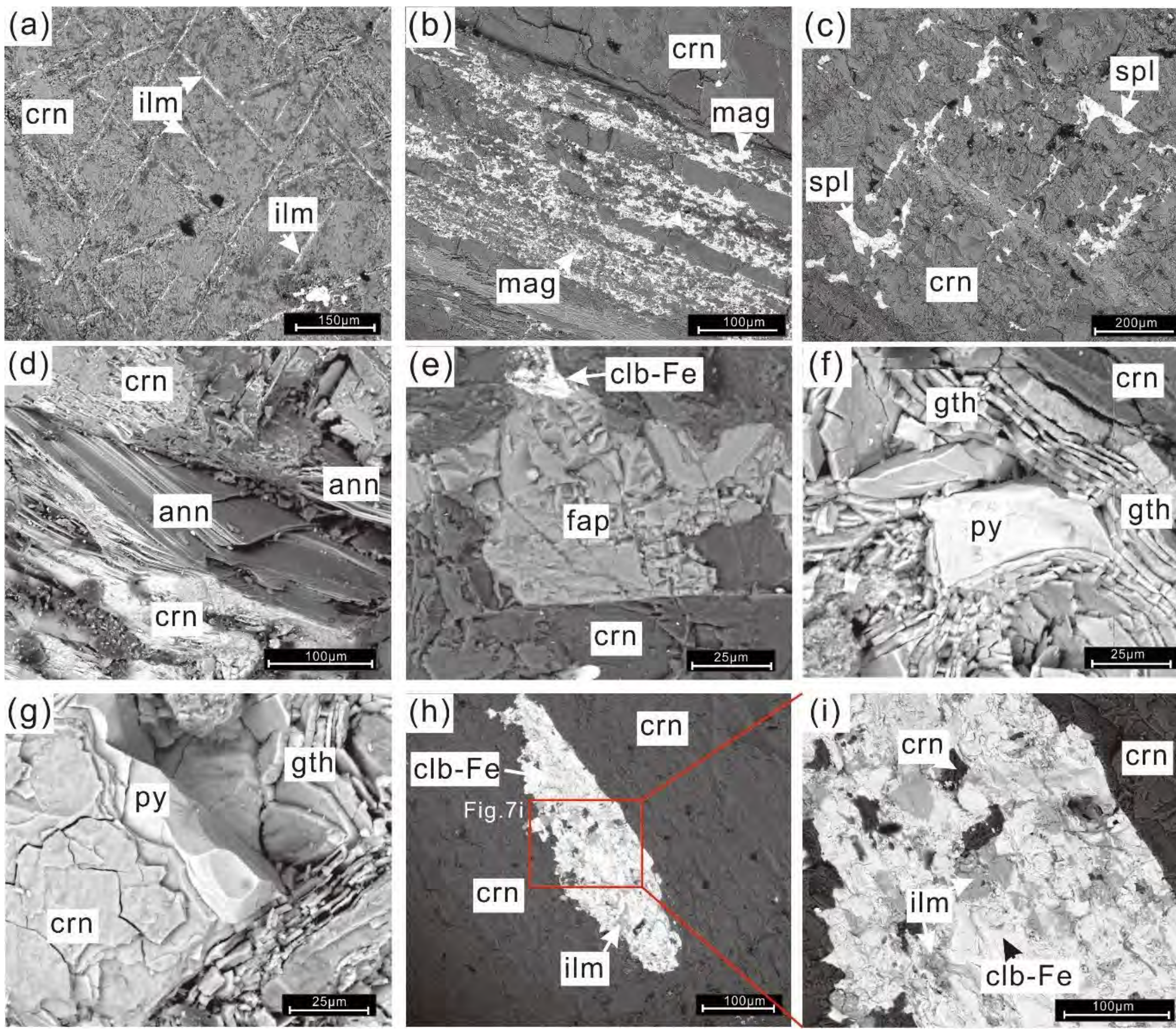

FIGURE 7. Back scattered electron images (BSE) showing secondary mineral inclusions in Yushishan corundum. (a) Fine-veined ilmenite occurring in three groups of thin veins; (b) Strips of magnetite; (c) Irregularly Zn-rich hercynite; (d) Lamellar annite; (e) Fluorapatite with irregular boundary; (f)-(g) Laminated goethite appeared at the edge of pyrite and pyrite gets curved boundary; (h)-(i) Ilmenite intergrowth with columbite-(Fe) in patchy, gray is ilmenite and white is columbite-(Fe). Abbreviations: crn=corundum; ilm=ilmenite; mag=magnetite; spl=spinel; clb-Fe=columbite-(Fe); py=pyrite; gth=goethite; ann=annite.

This is the peer-reviewed, final accepted version for American Mineralogist, published by the Mineralogical Society of America.
The published version is subject to change. Cite as Authors (Year) Title. American Mineralogist, in press.
DOI: https://doi.org/10.2138/am-2022-8223. http://www.minsocam.org/

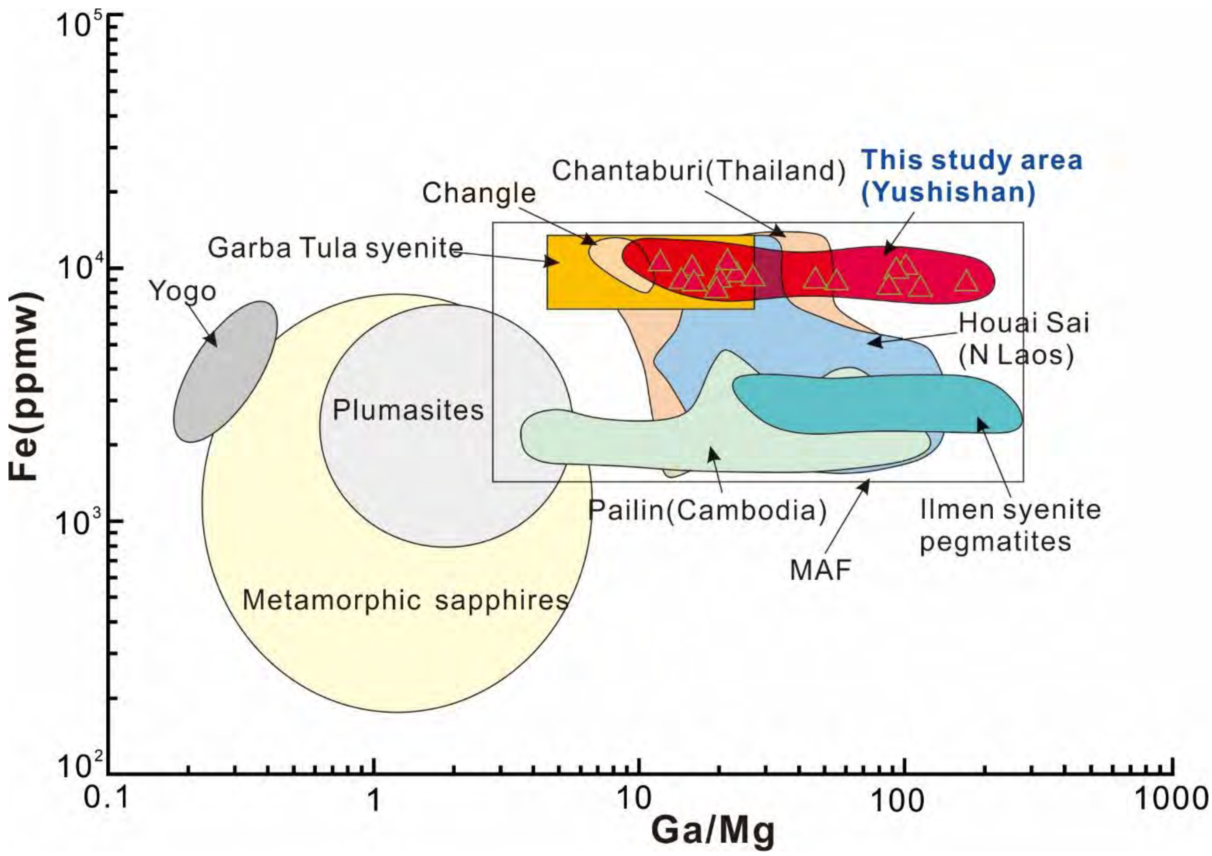

942

943 **FIGURE 8**. Illustration of Fe vs. Ga/Mg discrimination; MAF: main distribution range in Asia;
944 modified from Peucat et al. (2007), Zwaan et al. (2015) and Sorokina et al. (2017), green
945 triangle (red area) represents corundum test sites in Yushishan corundum.

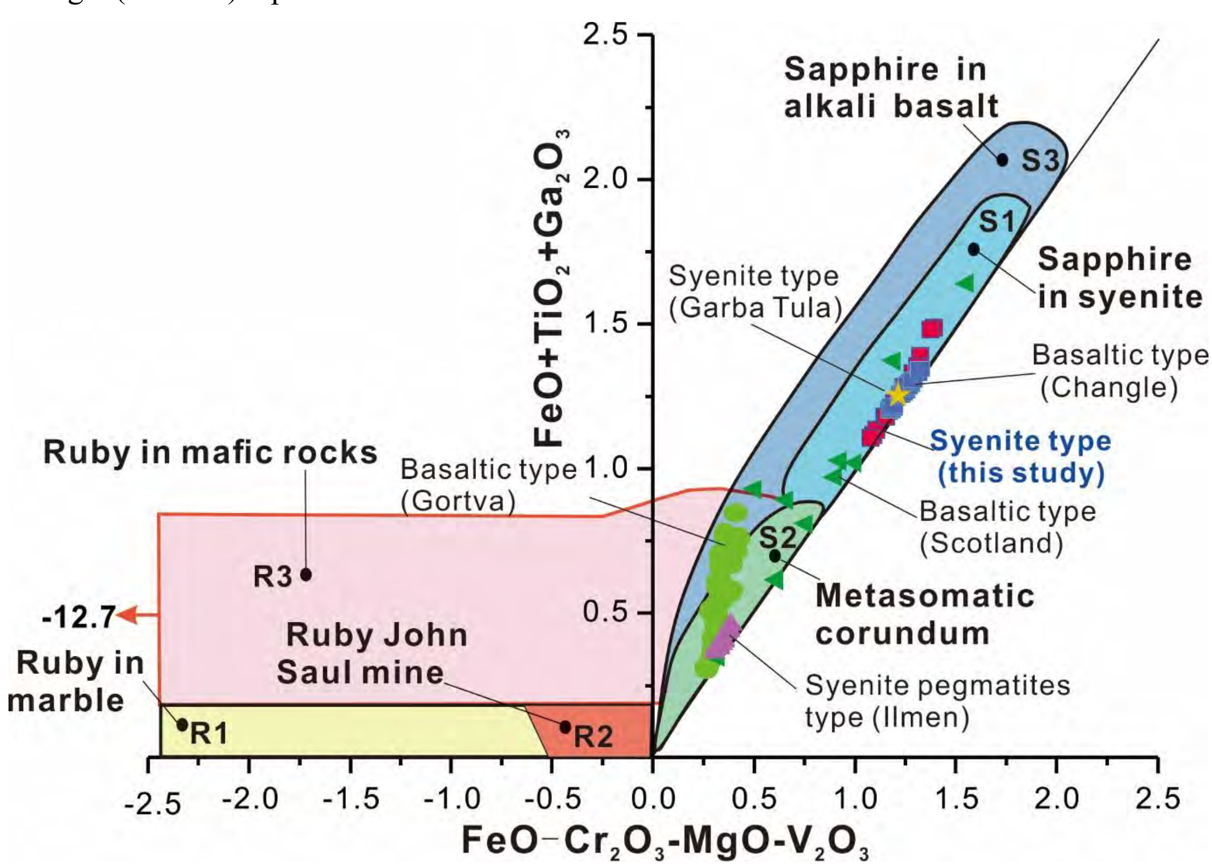

946

FIGURE 9. FeO-Cr_2O_3-MgO-V_2O_3 vs. FeO+TiO_2+Ga_2O_3 discriminant illustration (in wt.%) distinguishing corundum types of different genesis, modified from Giuliani et al. (2014b). The following different types of corundum are shown: (1) Sapphires of syenite type from Garba Tula (yellow star) (Peucat et al. 2007); (2) Sapphires of basaltic type from Changle (blue square) (Kong et al., 2017); (3) Sapphires of basaltic type from Scotland (green triangle) (Aspen et al. 1990); (4) Sapphires of basaltic type from Gortva (green circle) (Uher et al., 2012); (5) Sapphires of syenite pegmatites type from Ilmen (purple triangle) (Sorokina et al. 2017); (5) Corundum of syenite type from Yushishan (red square) (this study).

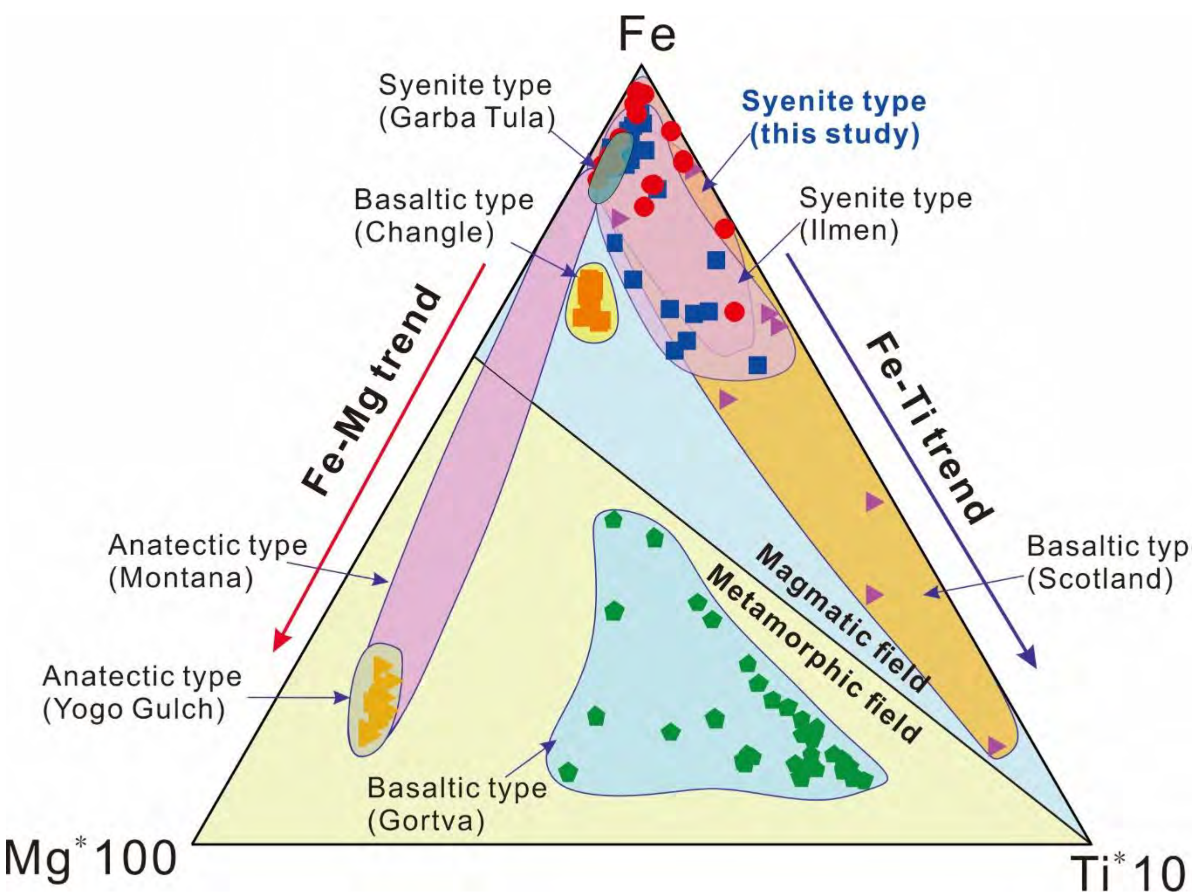

FIGURE 10. Fe-Mg-Ti discriminant illustration from trace element of corundum of different origins modified from (Peucat et al. 2007). The following different types of corundum are shown: (1) Sapphires of syenite type from Garba Tula (light green area) (Peucat et al. 2007); (2) Sapphires of basaltic type from Changle (orange square) (Kong et al. 2017); (3) Sapphires of basaltic type from Scotland (purple triangle) (Aspen et al. 1990); (4) Sapphires of basaltic type from Gortva (green pentagon) (Uher et al., 2012); (5) Sapphires of syenite pegmatites type from Ilmen (blue square) (Sorokina et al. 2017); (6) Sapphires of anatectic type from Montana (purple area) (Palke et al. 2017); (6) Sapphires of anatectic type from Yogo Gulch (yellow triangle) (Palke et al. 2016); (7) Corundum of syenite type from Yushishan (red circle) (this study);

966 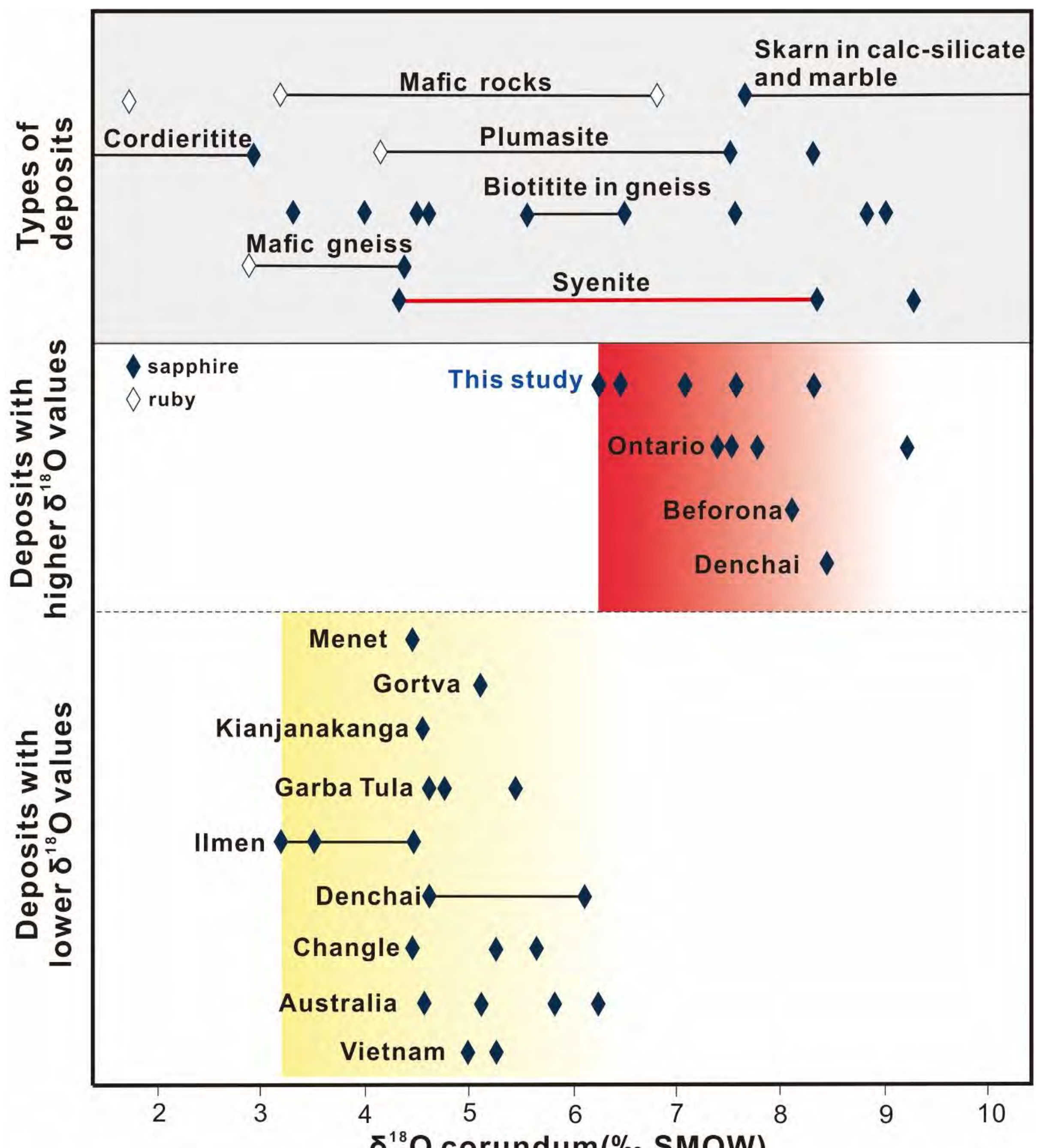

967 **FIGURE 11**. Comparison of the range of oxygen isotope values of corundum in syenite,
968 monzonite and anorthoclase, and sapphire xenocrysts in alkali basalt from different regions of
969 the world; black rhombus represents sapphire and white rhombus represents ruby; The range
970 of oxygen isotope delineation of corundum is from Giuliani et al. 2005,2007 (gray area).